AGU PUBLICATIONS

JGR

Journal of Geophysical Research: Solid Earth

RESEARCH ARTICLE

10.1002/2017JB014691

**Key Points:**
- A new probabilistic inversion tool based on 3-D forward operator was developed to probe mantle electrical conductivity
- We inverted new high-quality observatory data for local 1-D conductivity profiles that reveal significant lateral variations in the mantle
- Detected variations in conductivity imply variations of transition zone water content, temperature, and presence of melt

**Supporting Information:**
- Supporting Information S1

**Correspondence to:**
F. D. Munch,
federico.munch@erdw.ethz.ch

**Citation:**
Munch, F. D., Grayver, A. V., Kuvshinov, A. V., & Khan, A. (2018). Stochastic inversion of geomagnetic observatory data including rigorous treatment of the ocean induction effect with implications for transition zone water content and thermal structure. *Journal of Geophysical Research: Solid Earth*, *123*. https://doi.org/10.1002/2017JB014691

Received 12 JUL 2017
Accepted 8 DEC 2017
Accepted article online 13 DEC 2017



# Stochastic Inversion of Geomagnetic Observatory Data Including Rigorous Treatment of the Ocean Induction Effect With Implications for Transition Zone Water Content and Thermal Structure

**F. D. Munch[1], A. V. Grayver[1], A. Kuvshinov[1], and A. Khan[1]**

[1] Institute of Geophysics, ETH Zurich, Zurich, Switzerland

**Abstract** In this paper we estimate and invert local electromagnetic (EM) sounding data for 1-D conductivity profiles in the presence of nonuniform oceans and continents to most rigorously account for the ocean induction effect that is known to strongly influence coastal observatories. We consider a new set of high-quality time series of geomagnetic observatory data, including hitherto unused data from island observatories installed over the last decade. The EM sounding data are inverted in the period range 3–85 days using stochastic optimization and model exploration techniques to provide estimates of model range and uncertainty. The inverted conductivity profiles are best constrained in the depth range 400–1,400 km and reveal significant lateral variations between 400 km and 1,000 km depth. To interpret the inverted conductivity anomalies in terms of water content and temperature, we combine laboratory-measured electrical conductivity of mantle minerals with phase equilibrium computations. Based on this procedure, relatively low temperatures (1200–1350°C) are observed in the transition zone (TZ) underneath stations located in Southern Australia, Southern Europe, Northern Africa, and North America. In contrast, higher temperatures (1400–1500°C) are inferred beneath observatories on islands, Northeast Asia, and central Australia. TZ water content beneath European and African stations is ∼0.05–0.1 wt %, whereas higher water contents (∼0.5–1 wt %) are inferred underneath North America, Asia, and Southern Australia. Comparison of the inverted water contents with laboratory-constrained water storage capacities suggests the presence of melt in or around the TZ underneath four geomagnetic observatories in North America and Northeast Asia.

## 1. Introduction

Inferring the internal structure of the Earth is a key aspect for understanding its origin, evolution, and dynamics. In this regard, geophysical techniques such as seismic, geodetic, gravimetric, and electromagnetic (EM) studies play prominent roles because of their ability to sense structure at depth. In particular, EM studies aim at mapping electrical conductivity variations in the Earth. Electrical conductivity is sensitive to temperature, chemical composition, oxygen fugacity, water content, and the presence of melt (e.g., Karato & Wang, 2013; Park & Ducea, 2003; Yoshino, 2010). Hence, mapping electrical conductivity in turn enables constraining chemistry, mineralogy, and physical structure of the lithosphere and mantle (e.g., Deschamps & Khan, 2016; Dobson & Brodholt, 2000; Fullea et al., 2011; Khan et al., 2006; Pommier, 2014; Toffelmier & Tyburczy, 2007; Xu et al., 2000). For instance, global-scale (Kelbert et al., 2009; Semenov & Kuvshinov, 2012; Sun et al., 2015; Tarits & Mandéa, 2010) and semiglobal-scale (e.g., Koyama et al., 2006, 2014; Shimizu et al., 2010) three-dimensional (3-D) EM inversions of long-period geomagnetic data reveal the presence of large-scale lateral heterogeneities in the mantle.

Although significant improvements have been achieved in the last years with the emergence of the first set of 3-D mantle conductivity models, 3-D global and semiglobal EM induction studies still face several challenges. First, because of the high computational cost of 3-D forward operators only a coarse model parameterization is currently feasible resulting in limited radial resolution. Second, the deterministic approaches hitherto used in 3-D EM inversion lack quantification of uncertainties in the recovered 3-D conductivity models. Finally, the obtained 3-D conductivity models have poor lateral resolution in many regions of the world, especially in the oceans, due to the extremely nonuniform distribution of geomagnetic observatories.

To improve the latter, considerable efforts have focused on improving global data coverage of ground-based geomagnetic observatories. In particular, several island geomagnetic observatories have been installed in the last decade (see next section). Availability of these new data provides an opportunity to study the deep electrical conductivity structure under hitherto unexplored regions of the Earth. Kuvshinov et al. (2002) showed that EM response functions in the form of local C-responses (Banks, 1969) are influenced by the presence of the conductive oceans at coastal and island observatories. Several correction schemes to isolate experimental C-responses from the influence of oceans have been proposed (Kuvshinov et al., 2005; Püthe, Kuvshinov, Khan, & Olsen, 2015; Utada et al., 2003, among others). However, due to the nonlinearity of the problem, the most consistent way to account for the ocean induction effect (OIE) is to model it simultaneously with the inversion. In particular, for the period range considered here, oceans can be approximated by a thin surface shell of known conductance. Semenov and Kuvshinov (2012) computed magnetic fields for conductance distributions with different lateral resolution concluding that a resolution of at least $1^\circ \times 1^\circ$ is necessary to accurately account for the OIE in the thin-shell approach. However, global 3-D EM studies typically exploit a lower lateral resolution to preserve computational efficiency. In such cases, an unaccounted-for OIE might be translated into spurious anomalies in the recovered conductivity images.

In the light of the aforementioned challenges, the main goal of this study is to map lateral variations of electrical conductivity in Earth's mantle by relying on a quasi 1-D stochastic inversion of local C-responses. In short, we estimate local C-responses at a number of worldwide geomagnetic observatories and invert these individually for a local 1-D conductivity profile in the presence of nonuniform oceans and continents. This quasi 1-D inversion allows us to (a) improve radial resolution of local 1-D conductivity models, (b) properly account for the OIE, and (c) quantify uncertainties of the recovered conductivity profiles.

In the following, we describe estimation of local C-responses from a new data set provided by the British Geological Survey (Macmillan & Olsen, 2013) that consists of cleaned-up time series of the Earth's magnetic field recorded at geomagnetic observatories distributed across the globe (section 2). Section 3 introduces rigorous and accurate modeling of the OIE by implementation of a surface conductance map with lateral variable resolution. Section 4 presents the inverse problem formulation based on a stochastic optimization and model exploration technique. The inverted conductivity models and estimated uncertainties are discussed in section 5 and interpreted in terms of variations in transition zone water content and temperature in section 6.

## 2. Data Analysis

### 2.1. Data Selection

While satellite data are becoming increasingly important for constraining the electrical conductivity structure of the Earth (Constable & Constable, 2004; Grayver et al., 2017; Kuvshinov & Olsen, 2006; Olsen et al., 2003; Püthe, Kuvshinov, Khan, & Olsen, 2015; Velímský, 2010, among others), ground-based observatory data remain a major input for global EM induction studies. However, as stated above, there are still major gaps in the geomagnetic observatory network, especially in oceanic areas and in the Southern Hemisphere. Over the last decade, a number of geomagnetic observatory projects have been initiated to improve the coverage by long-term measurements in oceanic regions. For instance, since 2007 GFZ (Helmholtz-Zentrum Potsdam) has been operating an observatory in the South Atlantic Ocean on St. Helena Island (Korte et al., 2009). In 2008, an observatory on Easter Island (South Pacific Ocean) was installed by the Institut de Physique du Globe de Paris (France) and Direccion Meteorologica de Chile (Chulliat et al., 2009). Since 2009 GFZ and the National Space Institute at the Technical University of Denmark have been operating an observatory on Tristan da Cunha Island in the South Atlantic Ocean (Matzka et al., 2009). The Institute of Geophysics, ETH Zurich (Switzerland), installed two observatories in the Indian Ocean: on Gan island, Maldives (in cooperation with Maldives Meteorological Service and National Geophysical Research Institute, Hyderabad, India), and on Cocos Island (in cooperation with Geoscience Australia). The data from these stations have, so far, not been used for studying mantle conductivity structure.

To support the analysis of pre-Swarm and Swarm satellite data, the British Geological Survey (BGS) has recently provided a database of quality-controlled observatory hourly mean values for the years 1997–2016. This new data set consists of definitive or close-to-definitive data derived from the World Data Center (WDC) for Geomagnetism (Edinburgh) for which any known discontinuity in the records (reported by the observatories in their annual mean values) have been corrected and poor-quality data removed (Macmillan & Olsen, 2013).

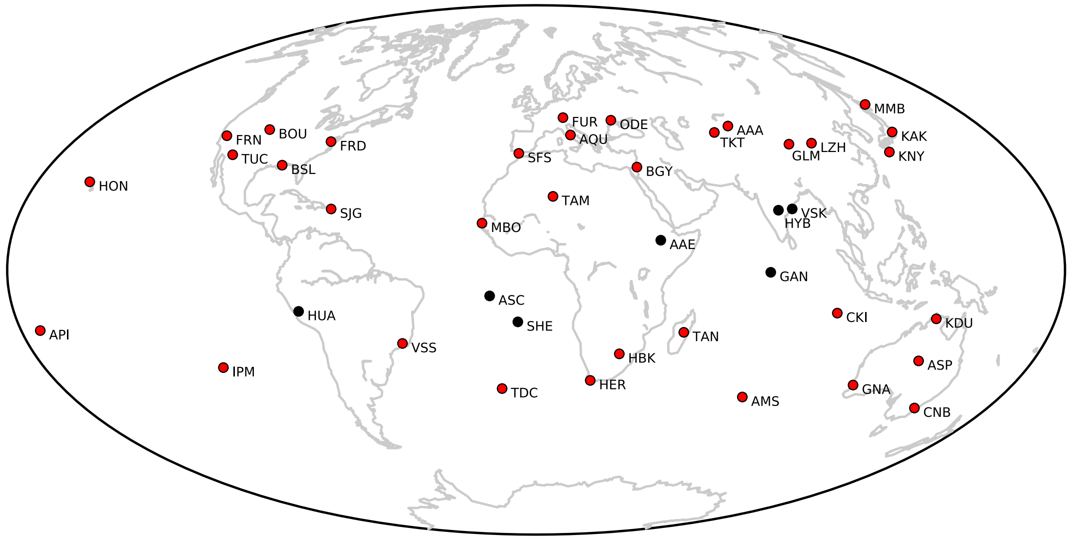


**Figure 1.** Distribution of geomagnetic observatories used in this study. Stations around dip equator (black) were not used in the inversion. Stations acronyms are defined in Table 1.

The BGS data set contains data from 171 geomagnetic observatories distributed worldwide. In selecting data for this study, we excluded data from (1) stations containing significant gaps or record lengths shorter than 3 years, (2) high-latitude stations that are known to be affected by the auroral current system (Fujii & Schultz, 2002; Semenov & Kuvshinov, 2012), and (3) on-land stations that have been frequently used in previous studies. Further, the selection procedure was applied so as to achieve as uniform global coverage as possible. To this end, we selected a subset of 39 high-quality stations from the BGS data set, including 6 new island geomagnetic observatories (IPM, TDC, ASC, SHE, GAN, and CKI) that are mainly located in the Southern Hemisphere. Additionally, we included definitive time series from the WDC data set for two geomagnetic observatories (TKT and ODE) that have been inoperative for the last 20 years. Locations of the selected stations are shown in Figure 1.

## 2.2. Estimation of Local C-Responses

Time series of the magnetic field, corrected for the main field and its secular variations, were used to determine local C-responses in the period range 3–85 days. Under the assumption that geomagnetic variations at the Earth's surface due to the magnetospheric ring current can be described via the first zonal harmonic in geomagnetic coordinates, C-responses are defined as (Banks, 1969)

$$C(\boldsymbol{r}_a, \omega) = -\frac{a \tan\theta}{2}\frac{Z(\boldsymbol{r}_a, \omega)}{H(\boldsymbol{r}_a, \omega)}, \tag{1}$$

where $Z \equiv -B_r$ and $H \equiv -B_\theta$ correspond to the respective radial and colatitudinal components of the geomagnetic field at location $\boldsymbol{r}_a = (r = a, \theta, \phi)$. The Earth's mean radius is denoted $a$, $\theta$ is the geomagnetic colatitude, and $\phi$ is the geomagnetic longitude. C-responses from observatory data were estimated using a section-averaging (e.g., Olsen, 1998) and iteratively reweighted least squares approach (e.g., Aster et al., 2005). Observational errors were determined using a jackknife estimator (e.g., Chave & Thomson, 1989). This method provides unbiased estimations of C-response uncertainties without assumptions about the statistical distribution of experimental errors (Efron, 1982). The main field and secular variation have been removed following Semenov and Kuvshinov (2012).

As an example, Figure 2 shows C-responses and squared coherencies estimated for Alice Springs (ASP) and Honolulu (HON) geomagnetic observatories. For comparison, C-responses estimated using raw time series, provided by INTERMAGNET, for the time window 1957–2007 (Semenov & Kuvshinov, 2012) are also plotted. The new C-responses are characterized by an increase in smoothness and squared coherency, as well as a decrease in experimental uncertainties.

Further, visual inspection of the estimated C-responses and squared coherencies revealed a decrease in coherency for stations close to the dip equator and polar regions. The latter is likely explained by the fact that

10.1002/2017JB014691

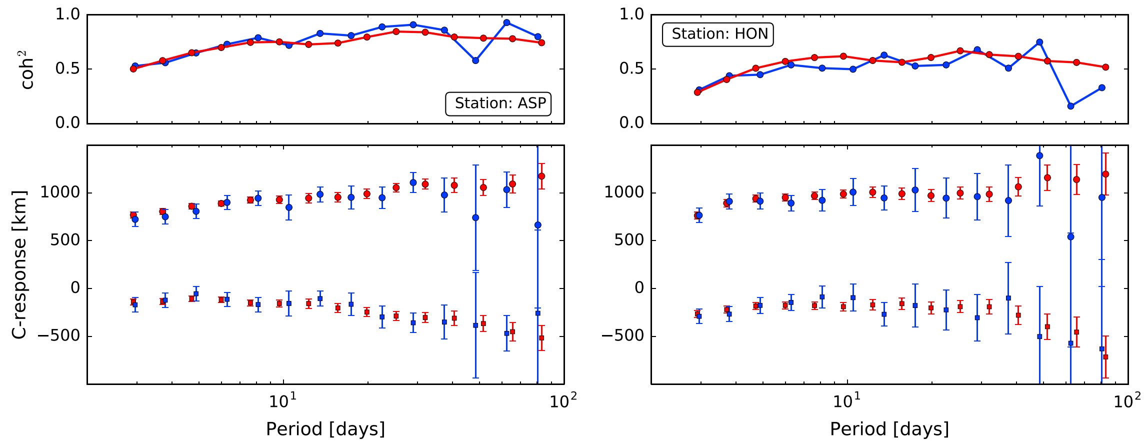


**Figure 2.** Real (positive) and imaginary (negative) parts of the experimental C-responses (bottom row) and squared coherencies coh$^2$ (top row) estimated in this study for Alice Springs (ASP) and Honolulu (HON) geomagnetic observatories using BGS data (red). Error bars indicate uncertainties of the experimental C-responses. For comparison, C-responses computed for the time window 1957–2007 (Semenov & Kuvshinov, 2012) are shown in blue.

**Table 1**
*Summary of Geomagnetic Observatories Acronyms, Names, Geodetic Geographic Coordinates (GG), Geomagnetic Coordinates (GM), and Time Interval of Measured Data*

| Code | Station | GG latitude (deg) | GG longitude (deg) | GM latitude (deg) | GM longitude (deg) | Data length |
|---|---|---|---|---|---|---|
| AAA | Alma Ata | 43.20 | 76.90 | 34.31 | 153.05 | 2006–2012 |
| AMS | Martin de Vivies | −37.80 | 77.57 | −46.00 | 145.09 | 1999–2008 |
| API | Apia | −13.80 | 188.22 | −15.22 | 263.05 | 2012–2016 |
| AQU | L'Aquila | 42.38 | 13.32 | 42.17 | 94.62 | 1998–2009 |
| ASP | Alice Springs | −23.77 | 133.88 | −32.42 | 208.61 | 1998–2016 |
| BGY | Bar Gyora | 31.72 | 35.09 | 28.14 | 112.73 | 2004–2010 |
| BOU | Boulder | 40.14 | 254.76 | 47.99 | 321.47 | 1998–2016 |
| BSL | Stennis Space Center | 30.35 | 270.36 | 39.58 | 340.48 | 1998–2005 |
| CKI | Cocos-Keeling Islands | −12.19 | 96.83 | −21.90 | 168.54 | 2012–2016 |
| CNB | Canberra | −35.32 | 149.36 | −42.71 | 226.94 | 1998–2016 |
| FRD | Fredericksburg | 38.20 | 282.63 | 47.88 | 354.05 | 1998–2016 |
| FRN | Fresno | 37.09 | 240.28 | 43.19 | 306.13 | 1998–2013 |
| FUR | Furstenfeldbruck | 48.17 | 11.28 | 48.13 | 94.64 | 1998–2015 |
| GLM | Golmud | 36.40 | 94.90 | 26.54 | 168.47 | 2010–2015 |
| GNA | Gnangara | −31.80 | 116.00 | −41.93 | 188.84 | 1998–2016 |
| HBK | Hartebeesthoek | −25.88 | 27.71 | −27.04 | 95.12 | 1998–2013 |
| HER | Hermanus | −34.43 | 19.23 | −33.98 | 84.02 | 1998–2016 |
| HON | Honolulu | 21.32 | 202.00 | 21.60 | 270.41 | 1998–2016 |
| IPM | Isla de Pascua | −27.20 | 250.58 | −19.13 | 325.37 | 2010–2015 |
| KAK | Kakioka | 36.23 | 140.18 | 27.37 | 208.95 | 1998–2016 |
| KDU | Kakadu | −12.69 | 132.47 | −21.55 | 206.07 | 1998–2016 |
| KNY | Kanoya | 31.42 | 130.88 | 21.89 | 200.75 | 1998–2016 |
| LZH | Lanzhou | 36.10 | 103.84 | 26.02 | 176.52 | 1998–2015 |
| ODE | Stepanovka | 46.78 | 30.88 | 19.76 | 57.89 | 1957–1991 |
| MBO | Mbour | 14.38 | 343.03 | 35.52 | 211.87 | 1998–2016 |
| MMB | Memambetsu | 43.91 | 144.19 | 43.71 | 112.71 | 1998–2016 |
| SFS | San Fernando | 36.67 | 354.06 | 39.73 | 73.38 | 1998–2016 |
| SJG | San Juan | 18.11 | 293.85 | 27.83 | 6.62 | 1998–2016 |
| TAM | Tamanrasset | 22.79 | 5.53 | 24.39 | 82.09 | 1998–2016 |
| TAN | Antananarivo | −18.92 | 47.55 | −23.48 | 116.46 | 1998–2004 |
| TDC | Tristan da Cunha | −37.07 | 347.69 | −31.52 | 54.3 | 2009–2016 |
| TKT | Tashkent | 41.33 | 69.62 | 33.30 | 146.35 | 1957–1981 |
| TUC | Tucson | 32.18 | 249.27 | 39.50 | 316.9 | 1998–2013 |
| VSS | Vassouras | −22.40 | 316.35 | −13.51 | 27.15 | 2001–2010 |

*Note.* Time series for years 1997–2016 were provided by the British Geological Survey (Macmillan & Olsen, 2013). Additionally, data for Tashkent (TKT) and Stepanovka (ODE) geomagnetic observatories were taken from the World Data Centre for Geomagnetism (Edinburgh).

the radial component of the magnetic field goes through zero at the dip equator. The former corresponds to violations of the source assumption because of the influence of polar currents, which cannot be represented using the first zonal harmonic only. In what follows, we therefore considered data from 34 stations that provide C-responses with an average squared coherency $>0.5$. Detailed information of the selected geomagnetic observatories (red dots in Figure 1) is summarized in Table 1.

## 3. Forward Problem and Model Parameterization

### 3.1. The Ocean Induction Effect

Oceans are large conductive bodies that cause significant perturbations in C-responses at coastal and island observatories for periods $<40$ days (cf. Kuvshinov et al., 2002). In the following section, we stress the importance of accounting for the OIE when working with C-responses at observatories near the coast. As an illustration of this, Figures 3a and 3b show observed and synthetic C-responses for Hermanus and Kakioka geomagnetic observatories. Two types of synthetic C-responses were calculated: $C^{1\text{D}}$ correspond to responses for a radially symmetric 1-D conductivity structure derived from satellite and ground-based data (Püthe, Kuvshinov, Khan, & Olsen, 2015) and $C^{1\text{D+shell}}$ denote responses estimated using the same 1-D conductivity model overlain by a surface layer accounting for conductivities relevant to the oceans and continents. The vertical and horizontal components of the magnetic field were calculated by numerically solving Maxwell's equations in spherical geometry (Kuvshinov, 2008). As expected, for a radially symmetric geometry (Weidelt, 1972), the real part of $C^{1\text{D}}$ monotonically increases with period, whereas the imaginary part is negative. However, the real part of the observed C-response at Hermanus observatory exhibits a nonmonotonic behavior, while the imaginary part changes sign. At Kakioka observatory, the behavior of the C-response follows the monotonic variation expected for a radially symmetric geometry, but it nonetheless appears to be affected by the ocean. Accounting for the OIE clearly improves the fit to the observed C-responses.

Figures 3c–3h show relative differences between 3-D and 1-D synthetic C-responses across Australia, Southern Africa, and Japan. These plots show that the OIE considerably distorts both real and imaginary parts of the C-responses. The largest distortions occur near the coasts where the imaginary part is influenced the most. This figure emphasizes that accounting for the OIE is essential when analyzing C-responses at coastal and island observatories.

Over the last decade, several approaches for correcting for the OIE have been proposed (Everett et al., 2003; Kuvshinov & Olsen, 2006; Püthe, Kuvshinov, Khan, & Olsen, 2015; Semenov & Kuvshinov, 2012, among others). For example, Utada et al. (2003) proposed the following (additive) correction:

$$C^{\text{exp,corr}}(\omega) = C^{\text{exp}}(\omega) + C^{1\text{D}}(\omega) - C^{1\text{D+shell}}(\omega), \tag{2}$$

where $C^{\text{exp}}$ corresponds to the observed experimental C-response, $C^{1\text{D}}$ is the synthetic C-response of a radially symmetric conductive Earth (without oceans), and $C^{1\text{D+shell}}$ is the C-response of the same radially symmetric conductive Earth overlain by an inhomogeneous shell (which approximates the distribution of oceans). Semenov and Kuvshinov (2012) reported that the effectiveness of the correction depends on the lateral resolution of the conductance distribution and the 1-D conductivity structure used for computing synthetic C-responses. The authors suggest that in order to accurately model the OIE using the thin-shell approximation, surface conductance should be described with a resolution of at least $1° \times 1°$ near the observation point. Furthermore, the conductivity structure must be representative of the region of interest. Although this correction succeeds in reducing the OIE in observed C-responses, it cannot completely remove the influence of ocean-induced fields because of the nonlinearity of the problem. Here we propose to properly account for the OIE by modeling the ocean/continent conductivity distribution as a thin shell of laterally varying surface conductance.

### 3.2. Model Parameterization

Our model parameterization consists of a thin spherical shell of known laterally varying surface conductance on top of a radially symmetric unknown conductivity profile (see Figure 4a). The thin-shell approximation is justified since for periods $>3$ days the penetration depth is much larger than the thickness of the oceanic layer. The surface conductance map was obtained by considering contributions from both seawater and sediments. The ocean conductance map was taken from Manoj et al. (2006) and incorporates bathymetry, salinity, temperature, and pressure variations. Conductance of the sediments was added for both continental and oceanic regions. The radially varying conductivity structure underneath consisted of 20 layers (50 km thick) between

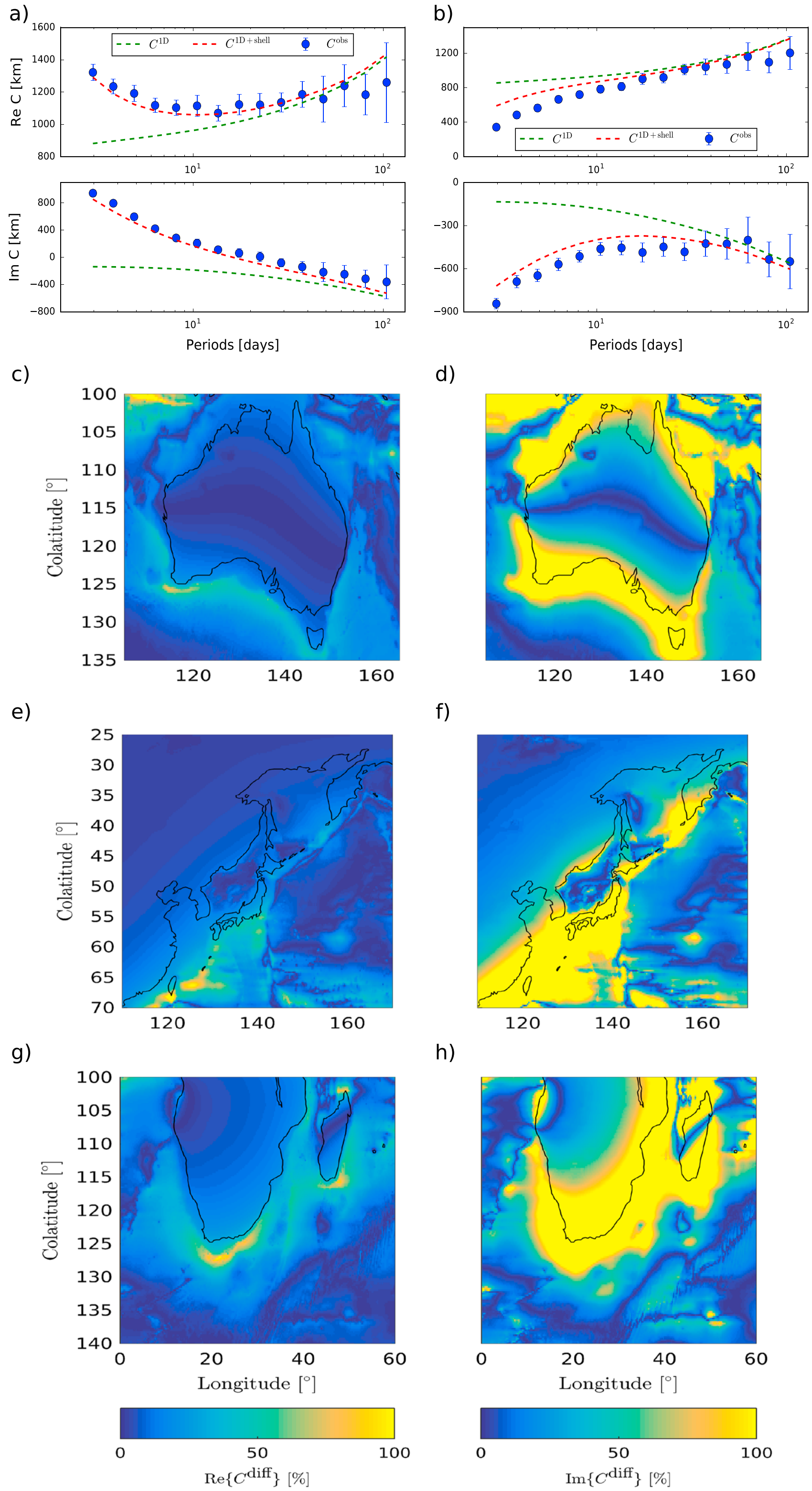


**Figure 3.** Real (left column) and imaginary (right column) parts of observed ($C^{obs}$ ) and synthetic C-responses for (a) Hermanus and (b) Kakioka geomagnetic observatories. Synthetic C-responses were calculated for a global average conductivity model (Püthe, Kuvshinov, Khan, & Olsen, 2015) with ($C^{1D+shell}$) and without ($C^{1D}$) ocean-induced fields. Figures 3c–3h show real (left column) and imaginary (right column) parts of the relative differences $C^{diff}$ between 3-D and 1-D synthetic C-responses for a period of 3 days across (c, d) Australia, (e, f) Japan, and (g, h) Southern Africa.

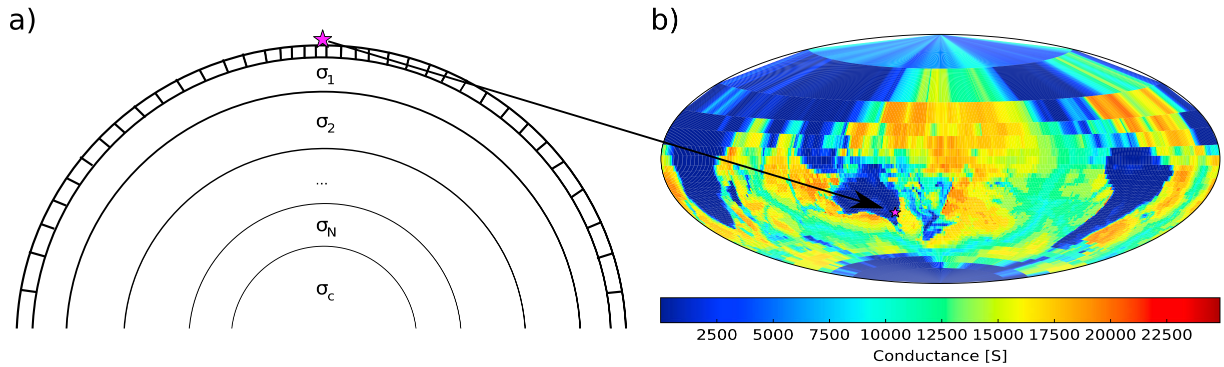


**Figure 4.** Model parameterization. (a) The Earth is parameterized as a thin spherical layer of laterally varying surface conductance (shown in Figure 4b) on top of a radially symmetric conductivity profile. The radial conductivity structure consists of 20 layers (50 km thick) in the depth range 0–1,000 km and 18 layers (100 km thick) in the depth range 1,000–2,900 km. (b) Example of nonuniform conductance map built for Canberra geomagnetic observatory.

the surface and 1,000 km depth, followed by 18 layers (100 km thick) down to the core-mantle boundary (~2,900 km depth). Vertical and horizontal components of the magnetic field for a 3-D spherical geometry were computed using the frequency domain 3-D integral equation (IE) solver (X3DG) of Kuvshinov (2008). Kelbert et al. (2014) showed that for the model setup considered in this work, the methods based on IE formulation require significantly shorter CPU times than methods based on either finite elements, finite differences, or spherical harmonic-finite elements.

Typically, IE modeling is performed using a surface conductance of laterally uniform resolution. In this paper the ocean/continent conductivity distribution was modeled using a surface conductance with variable lateral resolution. The reason for this is twofold. First, at every location, fields are weakly influenced by the conductance distribution located far away from the observation point. And second, X3DG implementation works such that the computational time depends quadratically on the number of cells in the latitudinal direction. Since in this study, C-responses were calculated at a single location, it was possible to use a nonuniform spacing without loss of accuracy. As a result, for every station a surface shell model was built. The conductance map had uniform (1°) resolution in longitude and nonuniform resolution in latitude. Latitudinal resolution was 1° in a region of ±20° around the observation site, and the grid size was increased by a factor of 1.6 for every 10° beyond. As an example, Figure 4b depicts the nonuniform surface conductance map built for Canberra geomagnetic observatory. This nonuniform conductance map reduces computation time (without loss of accuracy) by a factor of 17 compared to a uniform $1° \times 1°$ conductance distribution. Such a gain in performance allows us to utimately apply a stochastic inverse technique.

The choice of model parameterization and strategy to solve the inverse problem (section 4) was principally guided by our aim to overcome the aforementioned limitations existing in 3-D global studies.

## 4. Stochastic Inversion

Although significant improvements in the performance of X3DG have been achieved by introducing a nonuniform conductance distribution, the computational cost of the 3-D forward operator makes purely probabilistic inversion algorithms based on Markov chain Monte Carlo (McMC) (Tarantola, 2005) infeasible. Alternatively, deterministic derivative-based methods, such as quasi-Newton or Gauss-Newton, can be applied. However, for nonlinear inverse problems, these methods are highly dependent on the initial model, typically converge to a local minimum, require additional adjustments (e.g., Borsic & Adler, 2012) in the case of non-$L_2$ norms (Grayver & Kuvshinov, 2016), and do not provide uncertainty quantification. Therefore, our inverse problem formulation is based on a mixed scheme that combines a stochastic optimization technique known as Covariance Matrix Adaptation Evolution Strategy (CMAES) (Hansen & Ostermeier, 2001), with McMC methods (e.g., Mosegaard & Tarantola, 1995).

CMAES explores the model space globally and exhibits a remarkable robustness on ill-conditioned problems (Hansen et al., 2011). Although the use of CMAES in geophysics is not common, it has been implemented in recent studies as a global minimization method (Alvers et al., 2013; Diouane, 2014; Fonseca et al., 2014; Grayver et al., 2016, 2017; Shen et al., 2015) outperforming other techniques such as genetic algorithms and particle

Swarm optimization (Arsenault et al., 2013; Auger et al., 2009; Elshall et al., 2015). Additionally, Grayver and Kuvshinov (2016) showed that the use of CMAES for finding regions of low misfit can improve performance of conventional McMC methods.

In this section, we briefly present the algorithm; for details the reader is referred to Grayver and Kuvshinov (2016) and Hansen and Ostermeier (2001). Given $M$ unknown parameters, at every iteration the algorithm samples $\lambda = 4 + 3\ln M$ models from the current multivariate normal distribution and evaluates the misfit function. Then, the best $\lambda/2$ candidates are selected and used to update the distribution mean, step size, and covariance matrix. We use the CMAES algorithm to find the maximum posterior probability model, $\mathbf{m}_{\mathrm{MAP}}$, by solving the following optimization problem:

$$\mathbf{m}_{\mathrm{MAP}} = \underset{\mathbf{m}}{\operatorname{argmin}} \left[\phi_d(\mathbf{m}) + \beta\phi_m(\mathbf{m})\right], \tag{3}$$

where $\beta$ is a regularization parameter. The data ($\phi_d$) and model ($\phi_m$) terms are given by

$$\phi_d(\mathbf{m}) = \frac{1}{2}\sum_{i=1}^{N}\left|\frac{C^{\mathrm{obs}}(\omega_i) - C^{\mathrm{mod}}(\mathbf{m}, \omega_i)}{\delta C^{\mathrm{obs}}(\omega_i)}\right|^2, \tag{4}$$

and

$$\phi_m(\mathbf{m}) = \frac{1}{p}\sum_{i=1}^{M}\left|\nabla \mathrm{m}_i\right|^p, \tag{5}$$

where $N$ is the number of measurements, $C^{\mathrm{mod}}$ indicate modeled C-responses, whereas $C^{\mathrm{obs}}$ denote observed C-responses with uncertainties $\delta C^{\mathrm{obs}}$. Vector $\mathbf{m} = (\mathrm{m}_1, \mathrm{m}_2, \dots, \mathrm{m}_M)^T$ denotes the radial part of the conductivity model. Note that different norms were used for data and regularization terms. For the former, a common $L_2$ norm is chosen, whereas the latter is computed using $L_{1.5}$ norm ($p = 1.5$). This choice relies on studies performed by Grayver and Kuvshinov (2016) who showed that the $L_{1.5}$ norm provides a good balance between sharp conductivity contrasts ($L_1$ norm) and smooth models.

## 5. Results

### 5.1. Data Fit

The estimated C-responses were individually inverted to determine the most probable set of conductivities under each observatory. For each station, an L-curve analysis was performed to determine the optimal trade-off between data misfit and regularization terms (see supporting information). Figures 5 and 6 show observed and synthetic C-responses for the best-fit candidate model and final root-mean-square (RMS) error for each station. For most observatories considered in this work, both real and imaginary parts of the observed C-responses can be explained within experimental uncertainties using a 1-D conductivity profile overlain by a high-resolution thin shell. In particular, the nonmonotonic behavior of observed C-responses at coastal observatories is successfully reproduced. Although a certain complexity is neglected when reducing the data into a finite set of complex-valued C-responses, the model parameterization considered in this work appears reasonable for mid-latitude data.

The final conductivity models, on average, have a RMS error <0.95. There are four stations (CKI, IPM, KDU, and MBO) for which RMS error $\approx 2$. This increase is due to differences between the imaginary part of the observed and synthetic C-responses at short periods. As is shown in Figure 6 for Cocos Island (CKI) and Easter Island (IPM), synthetic C-responses explain the imaginary part of the observed C-responses at long periods ($T > 20$ days) but disagree at shorter periods. One can speculate that differences in the imaginary part of C-responses for short periods reflect either the presence of anomalously shallow structures or are artifacts arising from unmodeled OIE. In order to address the latter, we additionally computed C-responses using a surface conductance map on a $0.25° \times 0.25°$ grid for the best fit candidate models. No significant differences were observed between the C-responses for $1° \times 1°$ and $0.25° \times 0.25°$ grids. One may therefore argue that differences between observed and computed C-responses are due to anomalous structure in the upper mantle, unless the conductance distributions considered in this work do not account for certain small-scale local features in bathymetry or seawater conductivity.

### 5.2. Uncertainty Quantification

Uncertainty quantification of the final models is essential to evaluate the robustness and reliability of the retrieved conductivity structures. Studies based on deterministic approaches typically perform sensitivity


**Figure 5.** Real parts of observed (circles) and synthetic (dashed lines) C-responses for the best-fit conductivity models at the 34 geomagnetic observatories considered in the study (see Table 1). Uncertainties of observed C-responses are indicated by the error bars.

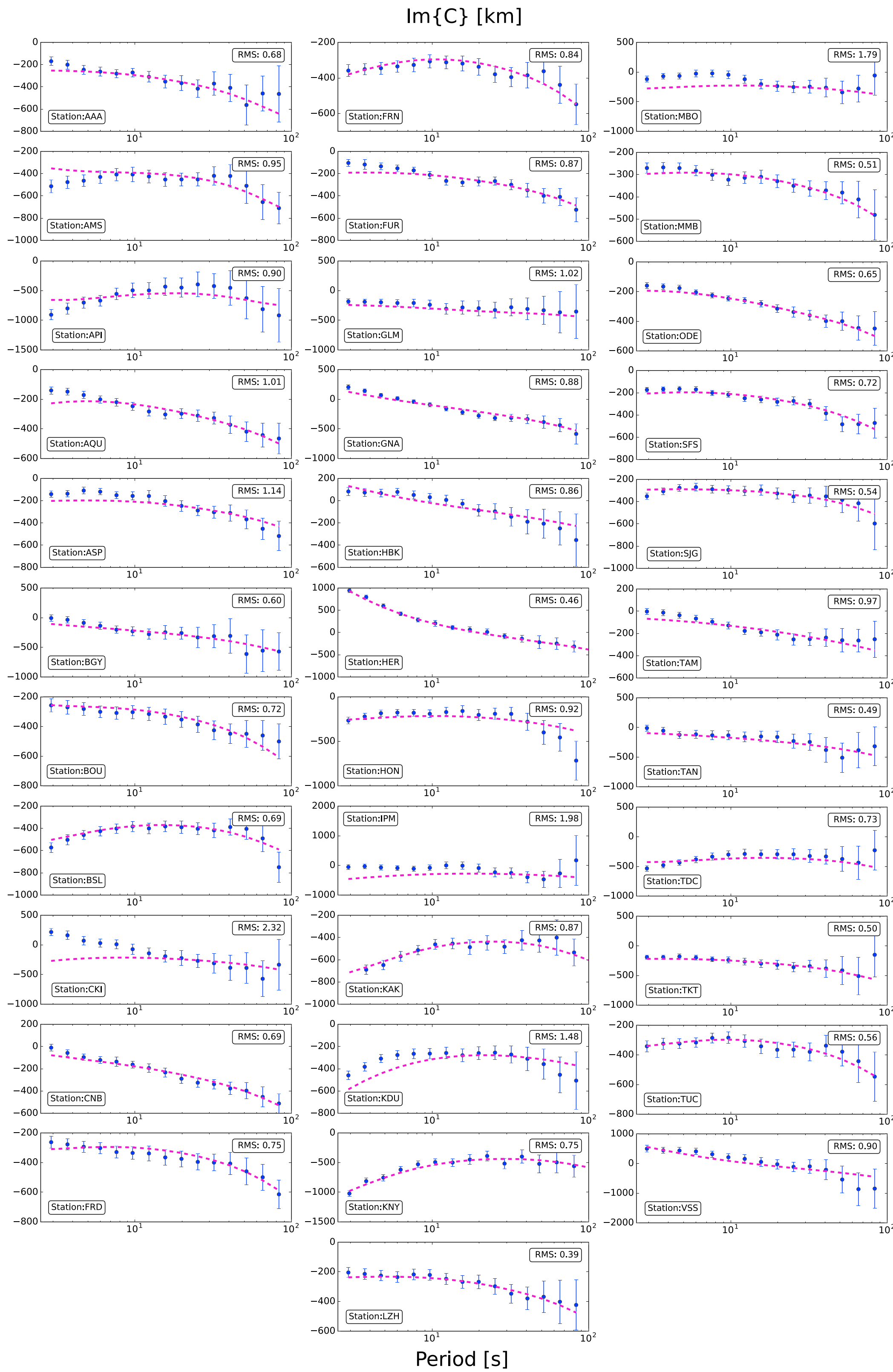


**Figure 6.** Imaginary parts of observed (circles) and synthetic (dashed lines) C-responses for the best-fit conductivity models at the 34 geomagnetic observatories considered in the study (see Table 1). Plots also include root-mean-square (RMS) error for real and imaginary parts of the responses. Uncertainties of observed C-responses are indicated by the error bars.

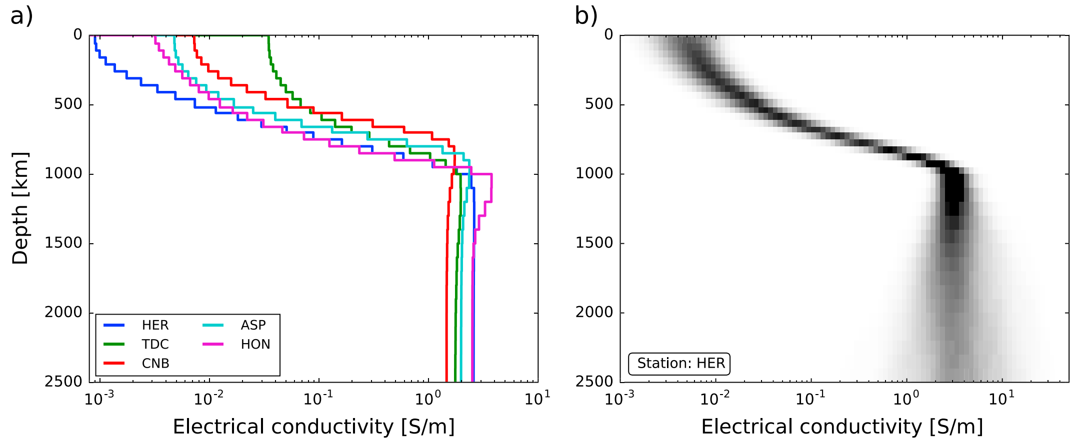


**Figure 7.** (a) Inverted conductivity models for Hermanus (HER), Tristan da Cunha (TDC), Honolulu (HON), Canberra (CNB), and Alice Springs (ASP) observatories. (b) Sampled posterior probability distribution for Hermanus geomagnetic observatory, with black indicating most probable and white least probable. Final posterior probability distributions for all analysed stations are shown in supporting information.

analysis based on applying small perturbations to the final conductivity model and comparing their effect on the computed responses (e.g., Baba et al., 2016; Meqbel et al., 2014). Although this strategy provides some insight, one can argue that the region of the model space sampled in such a sensitivity analysis is strongly study dependent (e.g., Trampert, 1998). Alternatively, a more consistent uncertainty quantification can be achieved by exploration of the model space around the best solution. Following this concept, model uncertainties are estimated using a McMC (e.g., Mosegaard & Tarantola, 1995) method. However, inversions based on McMC require a substantial amount of forward computations. The computational cost of the 3-D forward operator (even with the introduced laterally varying grid) makes model space exploration based on purely McMC methods prohibitive. Here we propose an alternative strategy where we explore the model space in the region around $\mathbf{m}_{MAP}$. First, we computed 1-D and 3-D synthetic C-responses for $\mathbf{m}_{MAP}$, followed by application of equation (2) to obtain experimental C-responses corrected for OIE. As mentioned in section 3.1, if the conductivity model $\mathbf{m}_{MAP}$ is a good estimation of the conductivity structure beneath the station, $C^{exp,corr}$ is largely isolated from the influence of the oceans. Following this, we performed an exploration of the model space around the most probable candidate using the Metropolis-Hastings (Hastings, 1970; Metropolis et al., 1953) algorithm considering $C^{exp,corr}$ as observed data and employed a 1-D forward operator to compute synthetic C-responses.

For each geomagnetic observatory, we performed a total of 1 million McMC iterations. The first 200,000 iterations were considered as burn-in period. Moreover, we analyzed the statistical independence of proposed models by estimating the cross correlation between candidates from successive realizations. In order to ensure the independence of proposed models (cross correlation $< 0.4$), only one candidate per 1,000 iterations was retained. The obtained models were used to estimate uncertainties of the electrical conductivity underneath each station assuming a log-normal distribution. Further, sampled conductivities were used to build a histogram of the marginal probability distribution for each layer. The sampled posterior probability distribution, shown in Figure 7b for a single station (HER), indicates increased uncertainty in the upper (<400 km depth) and lowermost mantle (>1,400 km depth). Therefore, and in agreement with previous studies (cf. Khan, Kuvshinov, & Semenov, 2011), the C-responses estimated in this work best constrain the conductivity structure in the depth range between 400 and 1,400 km.

### 5.3. Conductivity Models

In this section, we describe some of the most prominent features observed in the final conductivity models. To this end, Figure 7a shows the obtained conductivity structures for five geomagnetic observatories: Hermanus (HER), Tristan da Cunha (TDC), Honolulu (HON), Canberra (CNB), and Alice Springs (ASP). These five stations were chosen to highlight the significant variability of the final models. Additionally, a global average model derived from satellite and observatory data (Püthe, Kuvshinov, Khan, & Olsen, 2015) is shown for comparison. First, there are considerable differences in the first 400 km. Although the sensitivity analysis described in section 5.2 indicates low resolution in the uppermost mantle, the observed variability nonetheless suggests

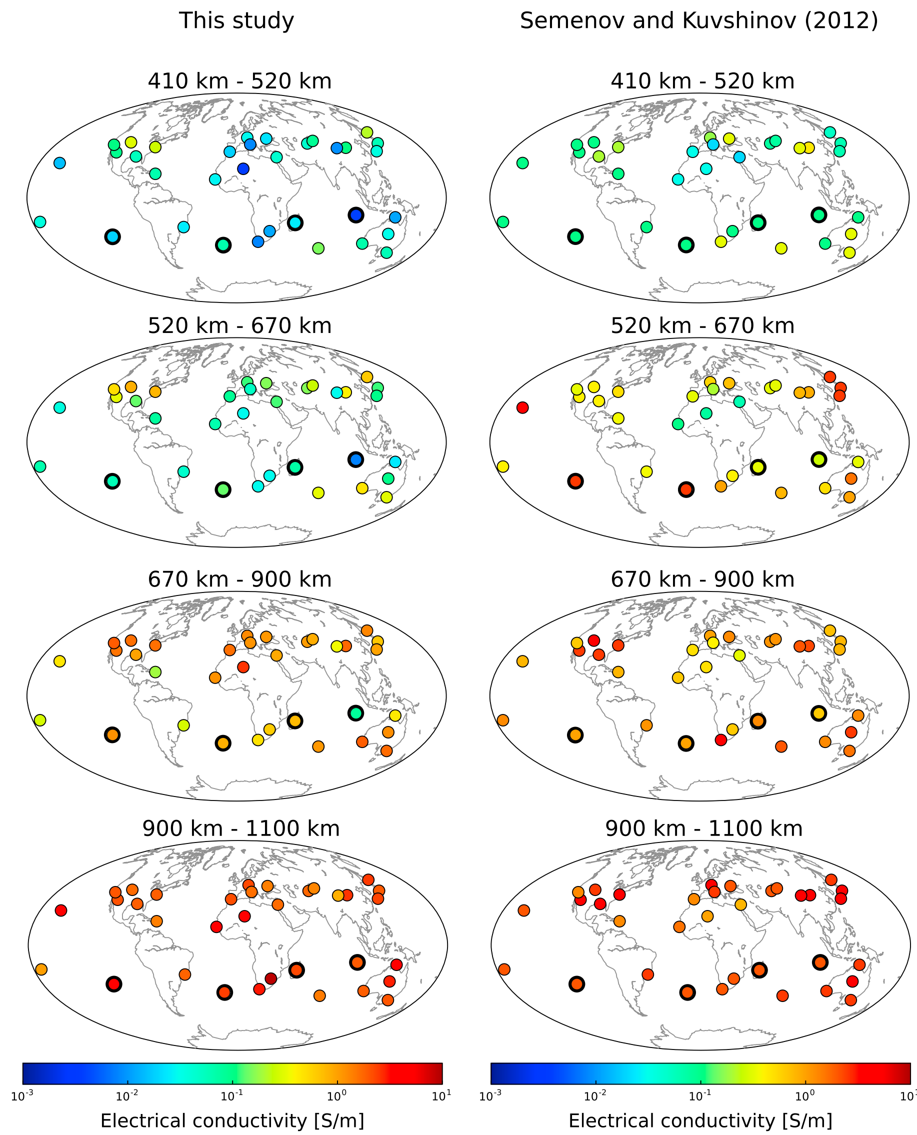


**Figure 8.** Conductivities recovered in this study (left column) averaged over four depth intervals: 410–520, 520–670, 670–900, and 900–1,100 km. For comparison, conductivities extracted from the 3-D conductivity model derived by Semenov and Kuvshinov (2012) are shown in the right column. Highlighted circles refer to island observatories that were not part of the Semenov and Kuvshinov (2012) data set.

that our results are sensitive to the bulk conductivity of the uppermost mantle. Second, significant lateral variability is observed in the depth range 400–1,100 km. And finally, variability is reduced in the lower mantle, reflecting more uniform structure in accordance with seismologic evidence (Schaeffer & Lebedev, 2015).

In order to visualize lateral variations in the inverted conductivity models, Figure 8 shows average conductivity values over four depth intervals: 410–520, 520–670, 670–900, and 900–1,100 km depth. Average conductivities for depths >1,100 km are not shown because of the aforementioned reduced lateral variation. For comparison, Figure 8 also depicts conductivity values extracted from the global 3-D conductivity model derived by Semenov and Kuvshinov (2012). The authors inverted local C-responses (period range 3–104 days) at 119 mid-latitude geomagnetic observatories to image the 3-D global electrical conductivity distribution in the mantle. They parameterized the depth range 410–1,600 km by five spherical layers of 110, 150, 230, 300, and 400 km thickness, respectively. All forward calculations were performed on a $3^\circ \times 3^\circ$ grid, whereas the lateral resolution of the inverse domain was chosen to be $9^\circ \times 9^\circ$. The observed C-responses were corrected for the ocean induction effect before inversion. Despite various differences in conductivity values, there is general similarity between both conductivity models. For instance, both models indicate small conductivity anomalies underneath Southern Europe and Northern Africa, whereas large conductivity anomalies are observed beneath North America and Northern Asia. The presence of a large conductivity anomaly underneath Northern Asia has also been reported by Kelbert et al. (2009) and more recently confirmed by Sun et al. (2015). Finally, both models suggest the presence of a large conductivity anomaly beneath Southern Australia. This feature is also consistent with the regional study performed by Koyama et al. (2014) and Koch and Kuvshinov (2015).

The most significant difference between our results and the model derived by Semenov and Kuvshinov (2012) concerns geomagnetic observatories located on islands. In the model of Semenov and Kuvshinov (2012), more conductive anomalies are found beneath island stations. This difference can be attributed to (a) lack of data from geomagnetic observatories located on Tamanrasset (TAM), Easter Island (IPM), Tristan da Cunha (TDC), and Cocos Island (CKI) (see Figure 8) and (b) the fact that the correction scheme applied by Semenov and Kuvshinov (2012) to account for the OIE is only approximate.

## 6. Thermochemical Interpretation of Conductivity Anomalies

### 6.1. Laboratory-Based Conductivity Profiles

In this section, we interpret the inverted conductivity anomalies in terms of transition zone thermal structure and water content. For this purpose, we compared the inverted conductivity models with laboratory-based conductivity profiles. We followed the approach described in detail in Khan (2016). Relative to Khan (2016), the conductivity database has been updated with recent measurements for clinopyroxene and Al-bearing bridgmanite. For brevity, only a summary is given here.

The laboratory-based conductivity profiles are computed from experimental measurements of mantle mineral conductivities in combination with mineral phase equilibrium computations. To compute phase equilibria, we employ the Gibbs free-energy minimization strategy described by Connolly (2009) and the self-consistent thermodynamic formulation of Stixrude and Lithgow-Bertelloni (2005) with parameters given by Stixrude and Lithgow-Bertelloni (2011), which predicts stable mineralogy (mineral modes) for a given pressure, temperature, and composition. The obtained mineral phase proportions are combined with laboratory-measured mineral conductivities to compute electrical conductivity as a function of pressure, temperature, and composition. The contribution from individual minerals to bulk conductivity is obtained by averaging using effective medium theory (Landauer, 1952) to produce a self-consistent solution. Khan (2016) analyzed different averaging strategies and found the self-consistent solution to be the only estimator that consistently lies within the Hashin-Shtrikman bounds (Hashin & Shtrikman, 1963). The latter bounds correspond to the narrowest possible restrictions that exist on an arbitrary isotropic multiphase system (Mavko et al., 2009).

Electrical conductivity is known to be highly sensitive to temperature and presence of water (e.g., Karato & Wang, 2013). In order to account for the influence of temperature and water content on hydrous minerals, we employ the electrical conductivity data from Yoshino and Katsura (2009) and Yoshino et al. (2012) for olivine, from Zhang et al. (2012) for orthopyroxene, from Zhao and Yoshino (2016) for clinopyroxene, from Yoshino and Katsura (2012) for wadsleyite, and from Yoshino, Manthilake, et al. (2008), Yoshino et al. (2012), and Yoshino and Katsura (2009) for ringwoodite. Additionally, we consider electrical conductivity data from Yoshino, Nishi, et al. (2008) for garnet, Katsura et al. (2007) for akimotoite, from Yoshino et al. (2011) for ferropericlase, from Xu et al. (2000) for calcium perovskite, and from Yoshino et al. (2016) for Al-bearing bridgmanite. Figure 9a summarizes conductivities for all minerals as a function of temperature, pressure, and water content. Following Khan (2016), we parameterize the water content of the mantle in terms of the water contents of olivine and wadsleyite. Water contents of clinopyroxene, orthopyroxene, and ringwoodite are estimated using the water partition coefficients based on measurements from Inoue et al. (2010) and Férot and Bolfan-Casanova (2012). Although we presently only use the measurements of Yoshino et al. because of their ready applicability we have to acknowledge that experimental disagreements currently exists with regard to the electrical conductivity of wadsleyite and ringwoodite. Dai and Karato (2009) measured the influence of temperature and water content on wadsleyite and ringwoodite reporting results that differ from those of Yoshino et al. Despite various efforts, the disagreement has not yet been resolved and the controversy remains (Karato, 2011; Yoshino & Katsura, 2013).

To illustrate the approach, Figure 9d shows the modal mineralogy and associated laboratory-based bulk electrical conductivity profiles for a pyrolitic mantle (Lyubetskaya & Korenaga, 2007) with a moderate amount

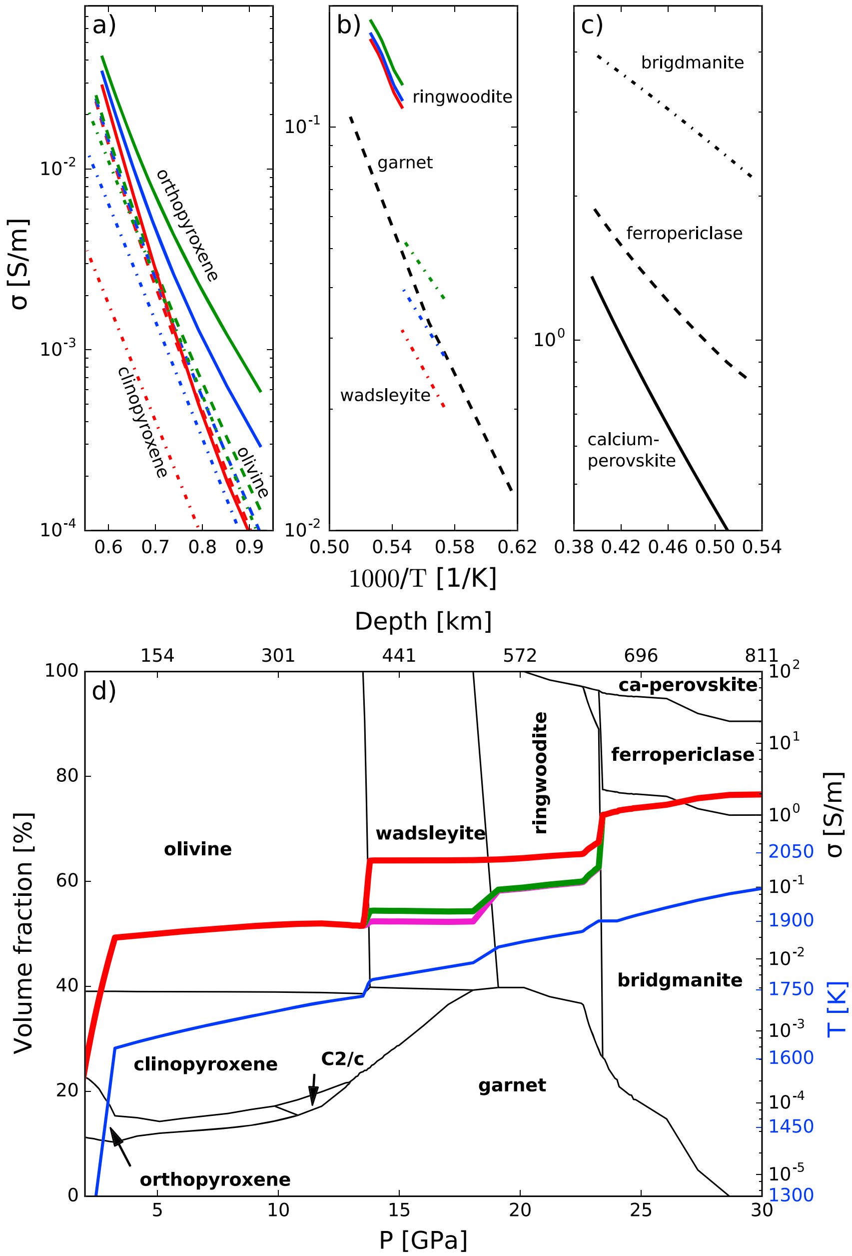


**Figure 9.** Summary of major (a) upper mantle, (b) transition zone, and (c) lower mantle single mineral electrical conductivities based on laboratory measurements as a function of inverse temperature, and water content. In Figure 9a colors scheme refers to differing water contents in nominally anhydrous upper mantle minerals: red, blue, and green indicate 0.001 wt %, 0.005 wt %, and 0.01 wt % of water, respectively. Figure 9b conductivity variations are computed for water contents of 0.01 wt % (red), 0.05 wt % (blue), and 0.1 wt % (green). (d) Modal mineralogy and bulk electrical conductivity for a pyrolitic mantle (composition from Lyubetskaya & Korenaga, 2007) with 0.01 wt % of water in olivine and different water contents in wadsleyite: 0.01 wt % (magenta), 0.1 wt % (green), and 1 wt % (red). The adiabatic geotherm (blue) is defined by the entropy of the lithology at a temperature of 1350°C at the base of a 100 km thick lithosphere.

of water (0.01 wt %) in olivine (Karato, 2011; Khan & Shankland, 2012) and different amounts of water in wadsleyite (0.01 wt %, 0.1 wt %, and 1 wt %). The composition is described using the CMFASNa model system comprising the oxides $CaO$-$MgO$-$FeO$-$Al_2O_3$-$SiO_2$-$Na_2O$, which account for ~98% of the mass of Earth's mantle (Anderson, 2007). The lithospheric temperature is computed by a linear gradient, whereas the sublithospheric mantle adiabat is defined by the entropy of the lithology at the base of the lithosphere (corresponding to 1350°C at 100 km depth). The pressure profile is obtained by integrating the load from the surface.

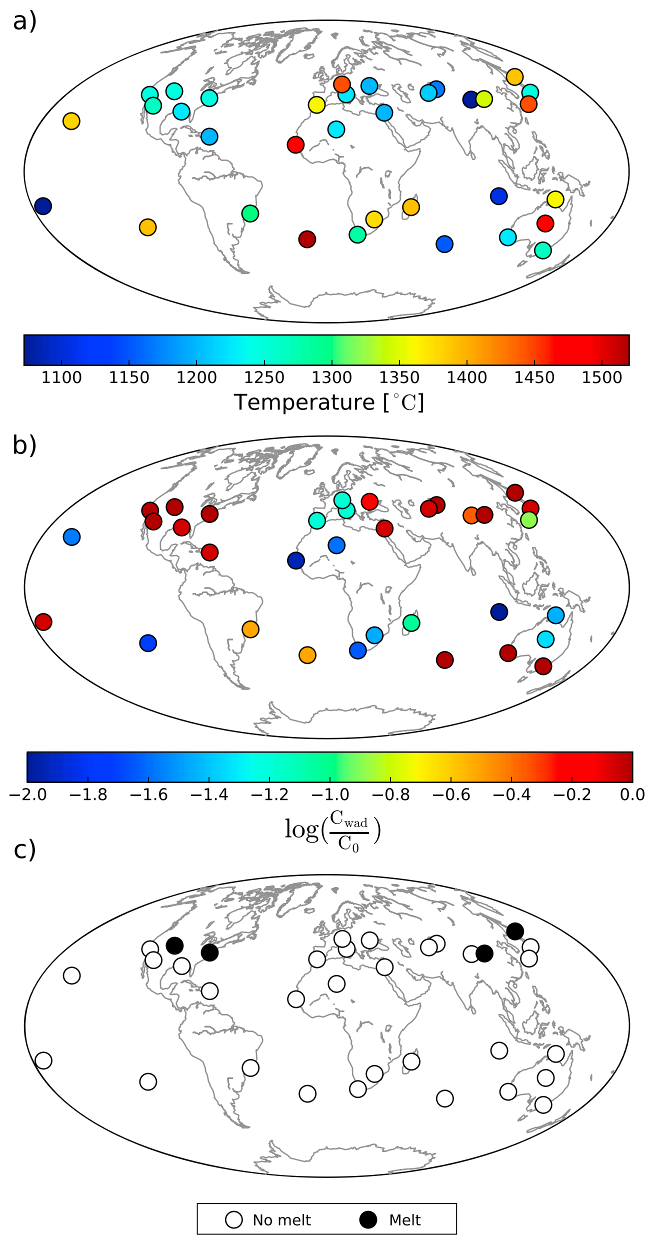


**Figure 10.** Spatial distribution of inverted transition zone temperatures (a) at 500 km depth and water content (b) in wadsleyite $C_{wad}$ ($C_0$ is equal to 1 wt %). The maps were obtained by converting the conductivity maps (Figure 8) to temperature and water content using the approach described in section 6. (c) Comparison of inverted water content with experimentally determined water storage capacities (Litasov et al., 2011) show locations where melt could potentially be present.

### 6.2. Transition Zone Temperature and Water Content

From Figure 9d, we observe that laboratory-based conductivity profiles implicitly incorporate discontinuities across the major phase transitions (olivine → wadsleyite, wadsleyite → ringwoodite, and ringwoodite → bridgmanite + ferropericlase), whereas the conductivity profiles retrieved from the inversion of C-responses (Figure 7a) are characterized by a continuous conductivity increase down to depths of ~1,000 km. These differences represent a fundamental challenge when comparing laboratory-based conductivity profiles with models retrieved from inversion of C-responses across the entire depth range. To overcome this complication, we focus our comparison on the depth ranges 400–650 km and 900–1,400 km.

We first performed several synthetic inversions (not shown here) to characterize compositional, thermal, and water content anomalies that can be successfully recovered given the conductivity uncertainties estimated in section 5.2. This synthetic analysis indicated that the conductivity profiles obtained from inversion of C-responses are mostly sensitive to variations in the thermal structure and water content of wadsleyite ($C_{wad}$). Based on this result, we computed 900 laboratory-based conductivity profiles for a pyrolitic mantle, where we varied thermal structure and water content between $T_0 \in [900°C, 1700°C]$ and $\log(C_{wad}/C_0) \in [-3, 1.5]$, where $T_0$ corresponds to the temperature at the base of a 100 km thick lithosphere and $C_0$ is a normalizing constant equal to 1 wt %. Conductivities were compared using a $L_2$ norm misfit function. The uncertainties on the final temperatures ($\delta T \sim 30°C$) and water contents ($\delta \log(C_{wad}/C_0) \sim 0.12$) were determined by visual inspection of the misfit surface. Figure 10 summarizes the water contents and temperatures in the transition zone (at 500 km depth) that best explain the observed electrical conductivity profiles. All final models explain the observations within uncertainties.

Relatively low transition zone temperatures (1200–1350°C) are found underneath stations located in Southern Australia, Southern Europe, Northern Africa, and North America. In contrast, higher transition zone temperatures (1400–1500°C) are obtained underneath several island observatories (TDC, IPM, HON, and TAN). These anomalies seem to be in agreement with higher potential temperatures beneath intraplate volcanic centers reported by Courtier et al. (2007). High-temperature anomalies are also observed beneath Northeast Asia (MMB and KNY) and the central region of Australia (ASP). Temperature variations in the transition zone across the globe span ~300–400°C and are in overall agreement with other regional studies (e.g., Cammarano & Romanowicz, 2007; Khan, Zunino, & Deschamps, 2011; Ritsema et al., 2009).

Regarding variations in transition zone water content, geomagnetic observatories in Europe and Africa are characterized by $C_{wad} \sim 0.05–0.1$ wt %, whereas higher water contents ($C_{wad} \sim 0.5–1$ wt %) are observed beneath stations located in North America, Asia, and Southern Australia. A dry transition zone below Europe has already been suggested by Utada et al. (2009) from joint inversion of electromagnetic and seismic tomographic models. Furthermore, temperatures and water contents obtained beneath ASP, FUR, HER, HON, LZH, and TUC are in general agreement with previous studies where a similar methodology was applied (Khan & Shankland, 2012; Khan, 2016). Based on experimental evidence of the water storage capacity (see below) of transition zone minerals (wadsleyite and ringwoodite), transition zone water content is higher than that of the upper mantle (olivine) ranging from ~0.1–1 wt % (Pearson et al., 2014; Peslier et al., 2017).

Mantle water content has to be analyzed in terms of the water storage capacities of mantle minerals. The water storage capacity is the maximum amount of water that a mineral or rock is able to retain at a given temperature and pressure without producing a hydrous fluid (e.g., Hirschmann et al., 2005). This implies that at locations where the water content exceeds the local storage capacity, hydrous melting ensues (e.g., Kohlstedt et al., 1996). Litasov et al. (2011) reported that the temperature dependence of the water storage capacity of wadsleyite (C) can be described by the exponential equation $C = 637.07\,e^{-0.0048T}$, where $T$ is in degrees Celsius. This provides an upper limit on the amount of water that can be stored in nominally anhydrous minerals in the transition zone. In the present work, we compared the estimated water storage capacities with the inverted water contents beneath each station. As shown in Figure 10c, we found that water storage capacities are only exceeded underneath four locations (BOU, FRD, MMB, and LZH). This suggests that thin melt layers (∼10–20 km thick) could possibly exist in and around the transition zone underneath these locations.

Although the presence of melt can potentially increase conductivity by several orders of magnitude (e.g., Pommier, 2014; Yoshino et al., 2010), the resolution of the conductivity profiles obtained here is not good enough to resolve these layers, if present. The current observation of melt has to be viewed in the context of the physical parameterization of the behavior of water-induced melting as observed experimentally by Litasov et al. (2011) and Férot and Bolfan-Casanova (2012). Thus, although data might not be able to accurately resolve a thin melt layer, physical conditions are such that melt is expected to appear.

It has been proposed that when material enriched in water is advected across the olivine → wadsleyite transition, it will undergo, due to differences in storage capacities between the two reservoirs, partial melting, and leave behind a residue with a water content similar to that of the upper mantle (Bercovici & Karato, 2003). In the water filter hypothesis by Bercovici and Karato (2003), this process is expected to occur globally rather than being restricted to localized water-rich upwellings. Although an accurate characterization of the melt layer is beyond the scope of this work, our results nonetheless suggest that the water filter hypothesis is only likely to be operative on a local/regional scale. Experimental and seismic evidence in support of localized melt layers on top of the transition zone (around 410 km depth) has also accumulated in the form of observations of low shear wave velocity anomalies at various locations of which many appear to be associated with areas where subduction has recently or is currently taking place (Freitas et al., 2017). The locations include western, central, and eastern United States (Courtier & Revenaugh, 2006; Jasbinsek & Dueker, 2007; Song et al., 2004; Song & Helmberger, 2006), Siberian platform (Vinnik & Farra, 2007), Arabian Plate (Vinnik et al., 2003), off the coast of Japan (Bagley et al., 2009; Revenaugh & Sipkinf, 1994), Southwest Pacific (Courtier & Revenaugh, 2007), and Afar Triple Junction in East Africa (Thompson et al., 2015).

The origin of water in the transition zone is likely due to water carried down with subducting plates along cold geotherms (e.g., Ohtani et al., 2004; Peslier et al., 2017; Schmidt & Poli, 1998) and due to upward percolation of hydrous melts from the lower mantle (e.g., Hirschmann, 2006), whose storage capacity is believed to be extremely low (e.g., Bolfan-Casanova et al., 2002, 2003). The extent to which this actually results in a water-enriched region in the transition zone is unclear. The water contents inferred here for the transition zone show large variability and are relatively modest (∼0.1 wt %) beneath geomagnetic observatories located in Europe, Africa, and Northern Australia but high (∼0.5–1 wt %) underneath stations in North America, Asia, and Southern Australia. These water contents are consistent with what has been experimentally determined (∼0.2 wt %) by Freitas et al. (2017). Since there is no evidence from geodynamic models that the “410 km” discontinuity acts as a barrier to mantle flow (e.g Christensen, 2001), material that is advected into the bottom of the upper mantle with passive upwellings may provide an explanation for how subducted water is being continuously drained from the transition zone and reenters the upper mantle and becomes remixed there. The lateral variations in water content that we observe beneath the various regions may therefore be due to subduction of water and possibly upwelling of hydrous melts that produces local water-rich regions in the transition zone.

Finally, it should be mentioned that the thermal structure and water contents derived in this work are subject to several assumptions. First, in the present thermodynamic model we preclude consideration of redox effects that might be expected to be important if native or ferric iron is present in Earth’s mantle. Second, $H_2O$, $TiO_2$, $Cr_2O_3$, and partial melt are not considered in the phase equilibria calculations. Third, although the pyrolitic model of Ringwood (1975) has become widely accepted as being representative of Earth’s average upper mantle composition, compositional perturbations from the pyrolitic model should still be explored (Khan et al., 2009). Finally, an inherent problem with the use of electrical conductivity for constraining transition zone water content and thermal structure is the trade-off between the parameters. Here a slight negative correlation between $T_0$ and $C_w$ is observed. Future studies will consider joint inversion of different geophysical observables in order to reduce this trade-off and help distinguishing thermal from compositional contributions (Afonso et al., 2013; Khan et al., 2009; Utada et al., 2009; Verhoeven et al., 2009, among others).

## 7. Concluding Remarks and Outlook

In this study, we estimated and inverted local C-responses (in the period range 3–85 days) at 34 midlatitude geomagnetic observatories to map lateral variations in the mantle electrical conductivity in the depth range 400–1,400 km. Novelties of this study include (a) usage of a new, high-quality data set including hitherto unused data from geomagnetic observatories installed on islands over the last 10 years; (b) rigorous and accurate modeling of the ocean induction effect; and (c) inversion of the data using a stochastic optimization technique. The ocean induction effect was rigorously accounted for by including a laterally varying surface conductance map in the computation of synthetic C-responses. Our inverse problem formulation was based on a mixed scheme that combines stochastic optimization (CMAES) with model space exploration (McMC) methods to estimate uncertainties of the retrieved models.

Uncertainty analysis demonstrates that the C-responses estimated in this work best constrain the conductivity structure in the depth range 400–1,400 km. However, our results are also sensitive to the bulk conductivity of the uppermost mantle. The obtained conductivity models indicate strong lateral variability for depths <1,100 km. The inverted conductivity structure was subsequently interpreted in terms of variations in thermal structure and water content in the transition zone. For this purpose, we compared the inverted conductivity models with laboratory-based conductivity profiles that were obtained by combining laboratory-measured electrical conductivity of mantle minerals with mantle mineralogy estimated using a self-consistent thermodynamic formulation. Transition zone temperature variations across the globe span ∼350°C. The transition zone underneath stations located in Europe and Africa is characterized by water contents around ∼0.05–0.1 wt %, while higher water contents (∼0.5–1 wt %) are observed beneath geomagnetic observatories situated in North America, Asia, and Southern Australia. Finally, we compared the obtained water contents with the water storage capacities measured by Litasov et al. (2011) to inquire about the possible presence of melt. The comparison suggests the presence of melt underneath four geomagnetic observatories in North America and Northeast Asia.

Some limitations of this work should be noted. First, high-latitude geomagnetic observatories were excluded from the analysis because of the influence of the auroral current system. Second, we described the field variations under consideration via the first zonal harmonic in geomagnetic coordinates. As a consequence, the potential complexity of the ring current system is not fully taken into account. Future work should focus on (a) including observatories at higher latitudes and (b) increasing the complexity with which the source mechanism is described. Isolating high-latitude data from the influence of the auroral current system could be partially addressed by the application of principal component analysis (Shore et al., 2016). A step toward handling more complex source models has been proposed by Püthe, Kuvshinov, and Olsen (2015). The authors introduced transfer functions that relate the local vertical magnetic field to the spherical harmonic coefficients describing the external part of the magnetic potential. However, this methodology implies that source and conductivity structure should be jointly determined. Deriving a suitable inversion scheme for this purpose is a challenge that will be considered in the future. Finally, resolution of lithospheric and uppermost mantle conductivity can be improved by jointly inverting multisource data. For instance, Grayver et al. (2017) showed that 1-D global conductivity models retrieved from joint inversion of tidal and magnetospheric signals better constrain the global conductivity structure of the upper mantle and transition zone.

**Acknowledgments**
The authors would like to thank the two anonymous reviewers for their constructive comments, which helped improve the manuscript. Time series of geomagnetic field used in this study are available at ftp://ftp.nerc-murchison.ac.uk/geomag/Swarm/AUX_OBS/hour/. This work was supported by grants from the Swiss National Science Foundation (SNF project 200021_159907) and from the Swiss National Supercomputing Centre (CSCS) under projects s660 and s767. Moreover, the authors would like to acknowledge the British Geological Survey (BGS), WDC Geomagnetism (Edinburgh), INTERMAGNET, and the many institutes around the world that operate magnetic observatories.

## References

Afonso, J., Fullea, J., Yang, Y., Connolly, J., & Jones, A. (2013). 3-D multi-observable probabilistic inversion for the compositional and thermal structure of the lithosphere and upper mantle. II: General methodology and resolution analysis. *Journal of Geophysical Research: Solid Earth*, *118*, 1650–1676. https://doi.org/10.1002/jgrb.50123

Alvers, M., Götze, H., Lahmeyer, B., Plonka, C., & Schmidt, S. (2013). Advances in 3D potential field modeling. In *75th EAGE Conference & Exhibition incorporating SPE EUROPEC 2013*.

Anderson, D. L. (2007). *New theory of the Earth*. Cambridge, UK: Cambridge University Press.

Arsenault, R., Poulin, A., Côté, P., & Brissette, F. (2013). Comparison of stochastic optimization algorithms in hydrological model calibration. *Journal of Hydrologic Engineering*, *19*(7), 1374–1384.

Aster, R., Borchers, B., & Thurber, C. (2005). *Parameter estimation and inverse problems*. Amsterdam: Elsevier Academic.

Auger, A., Hansen, N., Zerpa, J. M. P., Ros, R., & Schoenauer, M. (2009). Experimental comparisons of derivative free optimization algorithms. *SEA*, *5526*, 3–15.

Baba, K., Chen, J., Sommer, M., Utada, H., Geissler, W. H., Jokat, W., & Jegen, M. (2016). Marine magnetotellurics imaged no distinct plume beneath the Tristan da Cunha hotspot in the Southern Atlantic Ocean. *Tectonophysics*, *716*, 52–63. https://doi.org/10.1016/j.tecto.2016.09.033

Bagley, B., Courtier, A. M., & Revenaugh, J. (2009). Melting in the deep upper mantle oceanward of the Honshu slab. *Physics of the Earth and Planetary Interiors*, *175*(3), 137–144.

Banks, R. (1969). Geomagnetic variations and the electrical conductivity of the upper mantle. *Geophysical Journal International*, *17*(5), 457–487.

Bercovici, D., & Karato, S.-I. (2003). Whole-mantle convection and the transition-zone water filter. *Nature*, *425*(6953), 39–44.

Bolfan-Casanova, N., Keppler, H., & Rubie, D. C. (2003). Water partitioning at 660 km depth and evidence for very low water solubility in magnesium silicate perovskite. *Geophysical Research Letters*, *30*(17), 1905. https://doi.org/10.1029/2003GL017182

Bolfan-Casanova, N., Mackwell, S., Keppler, H., McCammon, C., & Rubie, D. (2002). Pressure dependence of H solubility in magnesiowüstite up to 25 GPa: Implications for the storage of water in the Earth's lower mantle. *Geophysical Research Letters*, *29*(10), 1449. https://doi.org/10.1029/2001GL014457

Borsic, A., & Adler, A. (2012). A primal–dual interior-point framework for using the $L_1$ or $L_2$ norm on the data and regularization terms of inverse problems. *Inverse Problems*, *28*(9), 095011.

Cammarano, F., & Romanowicz, B. (2007). Insights into the nature of the transition zone from physically constrained inversion of long-period seismic data. *Proceedings of the National Academy of Sciences of the United States of America*, *104*(22), 9139–9144.

Chave, A. D., & Thomson, D. J. (1989). Some comments on magnetotelluric response function estimation. *Journal of Geophysical Research*, *94*(14), 215–14.

Christensen, U. (2001). Geodynamic models of deep subduction. *Physics of the Earth and Planetary Interiors*, *127*(1), 25–34.

Chulliat, A., Lalanne, X., Gaya-Piqué, L. R., Truong, F., & Savary J. (2009). The new Easter Island magnetic observatory. In *Proceedings of the XIIIth IAGA workshop on geomagnetic observatory instruments, data acquisition and processing* (pp. 2009–1226).

Connolly, J. A. D. (2009). The geodynamic equation of state: What and how. *Geochemistry, Geophysics, Geosystems*, *10*(10), Q10014. https://doi.org/10.1029/2009GC002540

Constable, S., & Constable, C. (2004). Observing geomagnetic induction in magnetic satellite measurements and associated implications for mantle conductivity. *Geochemistry, Geophysics, Geosystems*, *5*, Q01006. https://doi.org/10.1029/2003GC000634

Courtier, A. M., Jackson, M. G., Lawrence, J. F., Wang, Z., Lee, C.-T. A., Halama, R., … Chen, W.-P. (2007). Correlation of seismic and petrologic thermometers suggests deep thermal anomalies beneath hotspots. *Earth and Planetary Science Letters*, *264*(1), 308–316.

Courtier, A. M., & Revenaugh, J. (2006). A water-rich transition zone beneath the eastern United States and Gulf of Mexico from multiple *ScS* reverberations. In S. D. Jacobsen & S. van der Lee (Eds.), *Earth's Deep Water Cycle* (pp. 181–193). Washington, DC: American Geophysical Union.

Courtier, A. M., & Revenaugh, J. (2007). Deep upper-mantle melting beneath the Tasman and Coral Seas detected with multiple *ScS* reverberations. *Earth and Planetary Science Letters*, *259*(1), 66–76.

Dai, L., & Karato, S.-I. (2009). Electrical conductivity of wadsleyite at high temperatures and high pressures. *Earth and Planetary Science Letters*, *287*(1), 277–283.

Deschamps, F., & Khan, A. (2016). Electrical conductivity as a constraint on lower mantle thermo-chemical structure. *Earth and Planetary Science Letters*, *450*, 108–119.

Diouane, Y. (2014). Globally convergent evolution strategies with application to Earth imaging problem in geophysics (PhD thesis). École Doctorale Mathématiques, Informatique et Télécommunications, Toulouse.

Dobson, D. P., & Brodholt, J. P. (2000). The electrical conductivity and thermal profile of the Earth's mid-mantle. *Geophysical Research Letters*, *27*(15), 2325–2328.

Efron, B. (1982). *The jackknife, the bootstrap and other resampling plans* (Vol. 38). Philadelphia: SIAM.

Elshall, A. S., Pham, H. V., Tsai, F. T.-C., Yan, L., & Ye, M. (2015). Parallel inverse modeling and uncertainty quantification for computationally demanding groundwater-flow models using covariance matrix adaptation. *Journal of Hydrologic Engineering*, *20*(8), 04014087.

Everett, M. E., Constable, S., & Constable, C. G. (2003). Effects of near-surface conductance on global satellite induction responses. *Geophysical Journal International*, *153*(1), 277–286.

Férot, A., & Bolfan-Casanova, N. (2012). Water storage capacity in olivine and pyroxene to 14 GPa: Implications for the water content of the Earth's upper mantle and nature of seismic discontinuities. *Earth and Planetary Science Letters*, *349*, 218–230.

Fonseca, R., Leeuwenburgh, O., Van den Hof, P., & Jansen, J.-D. (2014). Improving the ensemble-optimization method through covariance-matrix adaptation. *SPE Journal*, *20*(01), 155–168.

Freitas, D., Manthilake, G., Schiavi, F., Chantel, J., Bolfan-Casanova, N., Bouhifd, M. A., & Andrault, D. (2017). Experimental evidence supporting a global melt layer at the base of the Earth's upper mantle. *Nature Communications*, *8*(1), 2186.

Fujii, I., & Schultz, A. (2002). The 3D electromagnetic response of the Earth to ring current and auroral oval excitation. *Geophysical Journal International*, *151*(3), 689–709.

Fullea, J., Muller, M., & Jones, A. (2011). Electrical conductivity of continental lithospheric mantle from integrated geophysical and petrological modeling: Application to the Kaapvaal Craton and Rehoboth Terrane, southern Africa. *Journal of Geophysical Research*, *116*, B10202. https://doi.org/10.1029/2011JB008544

Grayver, A. V., & Kuvshinov, A. V. (2016). Exploring equivalence domain in nonlinear inverse problems using Covariance Matrix Adaption Evolution Strategy (CMAES) and random sampling. *Geophysical Journal International*, *205*, 971–987.

Grayver, A. V., Munch, F. D., Kuvshinov, A. V., Khan, A., Sabaka, T. J., & Tøffner-Clausen, L. (2017). Joint inversion of satellite-detected tidal and magnetospheric signals constrains electrical conductivity and water content of the upper mantle and transition zone. *Geophysical Research Letters*, *44*, 6074–6081. https://doi.org/10.1002/2017GL073446

Grayver, A. V., Schnepf, N. R., Kuvshinov, A. V., Sabaka, T. J., Manoj, C., & Olsen, N. (2016). Satellite tidal magnetic signals constrain oceanic lithosphere-asthenosphere boundary. *Science Advances*, *2*(9), e1600798.

Hansen, N., & Ostermeier, A. (2001). Completely derandomized self-adaptation in evolution strategies. *Evolutionary computation*, *9*(2), 159–195.

Hansen, N., Ros, R., Mauny, N., Schoenauer, M., & Auger, A. (2011). Impacts of invariance in search: When CMA-ES and PSO face ill-conditioned and non-separable problems. *Applied Soft Computing*, *11*(8), 5755–5769.

Hashin, Z., & Shtrikman, S. (1963). A variational approach to the theory of the elastic behaviour of multiphase materials. *Journal of the Mechanics and Physics of Solids*, *11*(2), 127–140.

Hastings, W. K. (1970). Monte Carlo sampling methods using Markov chains and their applications. *Biometrika*, *57*(1), 97–109.

Hirschmann, M. M. (2006). Water, melting, and the deep Earth $H_2O$ cycle. *Annual Review of Earth and Planetary Sciences*, *34*, 629–653.

Hirschmann, M. M., Aubaud, C., & Withers, A. C. (2005). Storage capacity of $H_2O$ in nominally anhydrous minerals in the upper mantle. *Earth and Planetary Science Letters*, *236*(1), 167–181.

Inoue, T., Wada, T., Sasaki, R., & Yurimoto, H. (2010). Water partitioning in the Earth's mantle. *Physics of the Earth and Planetary Interiors*, *183*(1), 245–251.

Jasbinsek, J., & Dueker, K. (2007). Ubiquitous low-velocity layer atop the 410-km discontinuity in the northern Rocky Mountains. *Geochemistry, Geophysics, Geosystems*, *8*, Q10004. https://doi.org/10.1029/2007GC001661

Karato, S.-I. (2011). Water distribution across the mantle transition zone and its implications for global material circulation. *Earth and Planetary Science Letters*, *301*(3), 413–423.

Karato, S.-I., & Wang, D. (2013). Electrical conductivity of minerals and rocks. In S. Karato (Ed.), *Physics and Chemistry of the Deep Earth* (pp. 145–182). Hoboken, NJ: John Wiley.

Katsura, T., Yokoshi, S., Kawabe, K., Shatskiy, A., Okube, M., Fukui, H., … Funakoshi, K.-i. (2007). Pressure dependence of electrical conductivity of (Mg, Fe) $SiO_3$ ilmenite. *Physics and Chemistry of Minerals*, *34*(4), 249–255.

Kelbert, A., Kuvshinov, A., Velímský, J., Koyama, T., Ribaudo, J., Sun, J., … Weiss, C. J. (2014). Global 3-D electromagnetic forward modelling: A benchmark study. *Geophysical Journal International*, *197*, 785–814.

Kelbert, A., Schultz, A., & Egbert, G. (2009). Global electromagnetic induction constraints on transition-zone water content variations. *Nature*, *460*(7258), 1003–1006.

Khan, A. (2016). On Earth's mantle constitution and structure from joint analysis of geophysical and laboratory-based data: An example. *Surveys in Geophysics*, *37*(1), 149–189.

Khan, A., Boschi, L., & Connolly, J. (2009). On mantle chemical and thermal heterogeneities and anisotropy as mapped by inversion of global surface wave data. *Journal of Geophysical Research*, *114*, B09305. https://doi.org/10.1029/2009JB006399

Khan, A., Connolly, J., & Olsen, N. (2006). Constraining the composition and thermal state of the mantle beneath Europe from inversion of long-period electromagnetic sounding data. *Journal of Geophysical Research*, *111*, B10102. https://doi.org/10.1029/2006JB004270

Khan, A., & Shankland, T. (2012). A geophysical perspective on mantle water content and melting: Inverting electromagnetic sounding data using laboratory-based electrical conductivity profiles. *Earth and Planetary Science Letters*, *317*, 27–43.

Khan, A., Kuvshinov, A., & Semenov, A. (2011). On the heterogeneous electrical conductivity structure of the Earth's mantle with implications for transition zone water content. *Journal of Geophysical Research*, *116*, B01103. https://doi.org/10.1029/2010JB007458

Khan, A., Zunino, A., & Deschamps, F. (2011). The thermo-chemical and physical structure beneath the North American continent from Bayesian inversion of surface-wave phase velocities. *Journal of Geophysical Research*, *116*, B09304. https://doi.org/10.1029/2011JB008380

Koch, S., & Kuvshinov, A. (2015). 3-D EM inversion of ground based geomagnetic Sq data. Results from the analysis of the Australian array (AWAGS) data. *Geophysical Journal International*, *200*, 1284–1296.

Kohlstedt, D., Keppler, H., & Rubie, D. (1996). Solubility of water in the $\alpha$, $\beta$ and $\gamma$ phases of $(Mg, Fe)_2$ $SiO_4$. *Contributions to Mineralogy and Petrology*, *123*(4), 345–357.

Korte, M., Mandea, M., Linthe, H.-J., Hemshorn, A., Kotzé, P., & Ricaldi, E. (2009). New geomagnetic field observations in the South Atlantic Anomaly region. *Annals of Geophysics*, *52*(1), 65–81.

Koyama, T., Khan, A., & Kuvshinov, A. (2014). Three-dimensional electrical conductivity structure beneath Australia from inversion of geomagnetic observatory data: Evidence for lateral variations in transition-zone temperature, water content and melt. *Geophysical Journal International*, *196*(3), 1330.

Koyama, T., Shimizu, H., Utada, H., Ichiki, M., Ohtani, E., & Hae, R. (2006). Water content in the mantle transition zone beneath the North Pacific derived from the electrical conductivity anomaly. In S. D. Jacobsen & S. van der Lee (Eds.), *Earth's Deep Water Cycle* (Vol. 168, pp. 171–179). Washington, DC: American Geophysical Union.

Kuvshinov, A. (2008). 3-D global induction in the oceans and solid Earth: Recent progress in modeling magnetic and electric fields from sources of magnetospheric, ionospheric and oceanic origin. *Surveys in Geophysics*, *29*(2), 139–186.

Kuvshinov, A., & Olsen, N. (2006). A global model of mantle conductivity derived from 5 years of CHAMP, ørsted, and SAC-C magnetic data. *Geophysical Research Letters*, *33*, L18301. https://doi.org/10.1029/2006GL027083

Kuvshinov, A., Utada, H., Avdeev, D., & Koyama, T. (2005). 3-D modelling and analysis of $Dst$ C-responses in the North Pacific Ocean region, revisited. *Geophysical Journal International*, *160*(2), 505–526.

Kuvshinov, A. V., Olsen, N., Avdeev, D. B., & Pankratov, O. V. (2002). Electromagnetic induction in the oceans and the anomalous behaviour of coastal C-responses for periods up to 20 days. *Geophysical Research Letters*, *29*(12), 1595. https://doi.org/10.1029/2001GL014409

Landauer, R. (1952). The electrical resistance of binary metallic mixtures. *Journal of Applied Physics*, *23*(7), 779–784.

Litasov, K. D., Shatskiy, A., Ohtani, E., & Katsura, T. (2011). Systematic study of hydrogen incorporation into Fe-free wadsleyite. *Physics and Chemistry of Minerals*, *38*(1), 75–84.

Lyubetskaya, T., & Korenaga, J. (2007). Chemical composition of Earth's primitive mantle and its variance: 1. Method and results. *Journal of Geophysical Research*, *112*, B03211. https://doi.org/10.1029/2005JB004223

Macmillan, S., & Olsen, N. (2013). Observatory data and the Swarm mission. *Earth, Planets and Space*, *65*(11), 1355–1362.

Manoj, C., Kuvshinov, A., Maus, S., & Lühr, H. (2006). Ocean circulation generated magnetic signals. *Earth, Planets and Space*, *58*(4), 429–437.

Matzka, J., Olsen, N., Maule, C. F., Pedersen, L. W., Berarducci, A., & Macmillan, S. (2009). Geomagnetic observations on Tristan da Cunha, South Atlantic Ocean. *Annal of Geophysics*, *52*(1), 97–105.

Mavko, G., Mukerji, T., & Dvorkin, J. (2009). *The rock physics handbook: Tools for seismic analysis of porous media*. Cambridge, UK: Cambridge University Press.

Meqbel, N. M., Egbert, G. D., Wannamaker, P. E., Kelbert, A., & Schultz, A. (2014). Deep electrical resistivity structure of the northwestern US derived from 3-D inversion of USArray magnetotelluric data. *Earth and Planetary Science Letters*, *402*, 290–304.

Metropolis, N., Rosenbluth, A. W., Rosenbluth, M. N., Teller, A. H., & Teller, E. (1953). Equation of state calculations by fast computing machines. *The Journal of Chemical Physics*, *21*(6), 1087–1092.

Mosegaard, K., & Tarantola, A. (1995). Monte Carlo sampling of solutions to inverse problems. *Journal of Geophysical Research*, *100*(B7), 12,431–12,447.

Ohtani, E., Litasov, K., Hosoya, T., Kubo, T., & Kondo, T. (2004). Water transport into the deep mantle and formation of a hydrous transition zone. *Physics of the Earth and Planetary Interiors*, *143*, 255–269.

Olsen, N. (1998). The electrical conductivity of the mantle beneath Europe derived from C-responses from 3 to 720 hr. *Geophysical Journal International*, *133*(2), 298–308.

Olsen, N., Vennerstrøm, S., & Friis-Christensen, E. (2003). Monitoring magnetospheric contributions using ground-based and satellite magnetic data. In C. Reigber, H. Lühr, & P. Schwintzer (Eds.), *First CHAMP mission results for gravity, magnetic and atmospheric studies* (pp. 245–250). Berlin: Springer.

Park, S. K., & Ducea, M. N. (2003). Can in situ measurements of mantle electrical conductivity be used to infer properties of partial melts? *Journal of Geophysical Research*, *108*(B5), 2270. https://doi.org/10.1029/2002JB001899

Peslier, A. H., Schönbächler, M., Busemann, H., & Karato, S. I. (2017). Water in the Earth's interior: Distribution and origin. *Space Science Reviews*, *212*(1–2), 743–810.

Pearson, D. G., Brenker, F. E., Nestola, F., McNeill, J., Nasdala, L., Hutchison, M. T., & Vekemans, B. (2014). Hydrous mantle transition zone indicated by ringwoodite included within diamond. *Nature*, *507*(7491), 221–224.

Pommier, A. (2014). Interpretation of magnetotelluric results using laboratory measurements. *Surveys in Geophysics*, *35*(1), 41–84.

Püthe, C., Kuvshinov, A., Khan, A., & Olsen, N. (2015). A new model of Earth's radial conductivity structure derived from over 10 yr of satellite and observatory magnetic data. *Geophysical Journal International*, *203*(3), 1864–1872.

Püthe, C., Kuvshinov, A., & Olsen, N. (2015). Handling complex source structures in global EM induction studies: From C-responses to new arrays of transfer functions. *Geophysical Journal International*, *201*(1), 318–328.

Revenaugh, J., & Sipkinf, S. (1994). Melt atop the 410-km mantle discontinuity. *Nature*, *369*, 474–476.

Ringwood, A. (1975). *Composition and petrology of the Earth's mantle*. US: McGraw-Hill Inc.

Ritsema, J., Xu, W., Stixrude, L., & Lithgow-Bertelloni, C. (2009). Estimates of the transition zone temperature in a mechanically mixed upper mantle. *Earth and Planetary Science Letters*, *277*(1), 244–252.

Schaeffer, A., & Lebedev, S. (2015). Global heterogeneity of the lithosphere and underlying mantle: A seismological appraisal based on multimode surface-wave dispersion analysis, shear-velocity tomography, and tectonic regionalization. In A. Khan & F. Deschamps (Eds.), *The Earth's Heterogeneous Mantle* (pp. 3–46). Cham: Springer.

Schmidt, M. W., & Poli, S. (1998). Experimentally based water budgets for dehydrating slabs and consequences for arc magma generation. *Earth and Planetary Science Letters*, *163*(1), 361–379.

Semenov, A., & Kuvshinov, A. (2012). Global 3-D imaging of mantle conductivity based on inversion of observatory C-responses—II. Data analysis and results. *Geophysical Journal International*, *191*(3), 965–992.

Shen, J., Lorenzo, J. M., White, C. D., & Tsai, F. (2015). Soil density, elasticity, and the soil-water characteristic curve inverted from field-based seismic *P*-and *S*-wave velocity in shallow nearly saturated layered soils. *Geophysics*, *80*(3), WB11–WB19.

Shimizu, H., Utada, H., Baba, K., Koyama, T., Obayashi, M., & Fukao, Y. (2010). Three-dimensional imaging of electrical conductivity in the mantle transition zone beneath the North Pacific Ocean by a semi-global induction study. *Physics of the Earth and Planetary Interiors*, *183*(1), 252–269.

Shore, R., Whaler, K., Macmillan, S., Beggan, C., Velímský, J., & Olsen, N. (2016). Decadal period external magnetic field variations determined via eigenanalysis. *Journal of Geophysical Research: Space Physics*, *121*, 5172–5184. https://doi.org/10.1002/2015JA022066

Song, T.-R. A., & Helmberger, D. V. (2006). Low velocity zone atop the transition zone in the western US from *S* waveform triplication. In S. D. Jacobsen & S. VanderLee (Eds.), *Earth's Deep Water Cycle* (Vol. 168, pp. 195–213). Washington, DC: American Geophysical Union.

Song, T.-R. A., Helmberger, D. V., & Grand, S. P. (2004). Low-velocity zone atop the 410-km seismic discontinuity in the northwestern United States. *Nature*, *427*(6974), 530–533.

Stixrude, L., & Lithgow-Bertelloni, C. (2005). Mineralogy and elasticity of the oceanic upper mantle: Origin of the low-velocity zone. *Journal of Geophysical Research*, *110*, B03204. https://doi.org/10.1029/2004JB002965

Stixrude, L., & Lithgow-Bertelloni, C. (2011). Thermodynamics of mantle minerals—II. Phase equilibria. *Geophysical Journal International*, *184*(3), 1180–1213.

Sun, J., Kelbert, A., & Egbert, G. (2015). Ionospheric current source modeling and global geomagnetic induction using ground geomagnetic observatory data. *Journal of Geophysical Research: Solid Earth*, *120*, 6771–6796. https://doi.org/10.1002/2015JB012063

Tarantola, A. (2005). *Inverse problem theory and methods for model parameter estimation*. Philadelphia: Society for Industrial and Applied Mathematics.

Tarits, P., & Mandéa, M. (2010). The heterogeneous electrical conductivity structure of the lower mantle. *Physics of the Earth and Planetary Interiors*, *183*(1), 115–125.

Thompson, D., Hammond, J., Kendall, J.-M., Stuart, G., Helffrich, G., Keir, D., … Goitom, B. (2015). Hydrous upwelling across the mantle transition zone beneath the Afar Triple Junction. *Geochemistry, Geophysics, Geosystems*, *16*, 834–846. https://doi.org/10.1002/2014GC005648

Toffelmier, D. A., & Tyburczy, J. A. (2007). Electromagnetic detection of a 410-km-deep melt layer in the southwestern United States. *Nature*, *447*(7147), 991–994.

Trampert, J. (1998). Global seismic tomography: The inverse problem and beyond. *Inverse Problems*, *14*(3), 371–385.

Utada, H., Koyama, T., Shimizu, H., & Chave, A. (2003). A semi-global reference model for electrical conductivity in the mid-mantle beneath the North Pacific region. *Geophysical Research Letters*, *30*(4), 1194. https://doi.org/10.1029/2002GL016092

Utada, H., Koyama, T., Obayashi, M., & Fukao, Y. (2009). A joint interpretation of electromagnetic and seismic tomography models suggests the mantle transition zone below Europe is dry. *Earth and Planetary Science Letters*, *281*(3), 249–257.

Velímský, J. (2010). Electrical conductivity in the lower mantle: Constraints from CHAMP satellite data by time-domain EM induction modelling. *Physics of the Earth and Planetary Interiors*, *180*(3), 111–117.

Verhoeven, O., Mocquet, A., Vacher, P., Rivoldini, A., Menvielle, M., Arrial, P.-A., … Van Hoolst, T. (2009). Constraints on thermal state and composition of the Earth's lower mantle from electromagnetic impedances and seismic data. *Journal of Geophysical Research*, *114*, B03302. https://doi.org/10.1029/2008JB005678

Vinnik, L., & Farra, V. (2007). Low *S* velocity atop the 410-km discontinuity and mantle plumes. *Earth and Planetary Science Letters*, *262*(3), 398–412.

Vinnik, L., Ravi Kumar, M., Kind, R., & Farra, V. (2003). Super-deep low-velocity layer beneath the Arabian Plate. *Geophysical Research Letters*, *30*(7), 1415. https://doi.org/10.1029/2002GL016590

Weidelt, P. (1972). The inverse problem of geomagnetic induction. *Journal of Geophysics*, *38*, 257–289.

Xu, Y., Shankland, T. J., & Poe, B. T. (2000). Laboratory-based electrical conductivity in the Earth's mantle. *Journal of Geophysical Research*, *105*(B12), 27,865–27,875.

Yoshino, T. (2010). Laboratory electrical conductivity measurement of mantle minerals. *Surveys in Geophysics*, *31*(2), 163–206.

Yoshino, T., & Katsura, T. (2009). Effect of iron content on electrical conductivity of ringwoodite, with implications for electrical structure in the transition zone. *Physics of the Earth and Planetary Interiors*, *174*(1), 3–9.

Yoshino, T., & Katsura, T. (2012). Re-evaluation of electrical conductivity of anhydrous and hydrous wadsleyite. *Earth and Planetary Science Letters*, *337*, 56–67.

Yoshino, T., & Katsura, T. (2013). Electrical conductivity of mantle minerals: Role of water in conductivity anomalies. *Annual Review of Earth and Planetary Sciences*, *41*, 605–628.

Yoshino, T., Ito, E., Katsura, T., Yamazaki, D., Shan, S., Guo, X., … Funakoshi, K.-I. (2011). Effect of iron content on electrical conductivity of ferropericlase with implications for the spin transition pressure. *Journal of Geophysical Research*, *116*, B04202. https://doi.org/10.1029/2010JB007801
Yoshino, T., Laumonier, M., McIsaac, E., & Katsura, T. (2010). Electrical conductivity of basaltic and carbonatite melt-bearing peridotites at high pressures: Implications for melt distribution and melt fraction in the upper mantle. *Earth and Planetary Science Letters*, *295*(3), 593–602.
Yoshino, T., Kamada, S., Zhao, C., Ohtani, E., & Hirao, N. (2016). Electrical conductivity model of Al-bearing bridgmanite with implications for the electrical structure of the Earth's lower mantle. *Earth and Planetary Science Letters*, *434*, 208–219.
Yoshino, T., Manthilake, G., Matsuzaki, T., & Katsura, T. (2008). Dry mantle transition zone inferred from the conductivity of wadsleyite and ringwoodite. *Nature*, *451*(7176), 326–329.
Yoshino, T., Nishi, M., Matsuzaki, T., Yamazaki, D., & Katsura, T. (2008). Electrical conductivity of majorite garnet and its implications for electrical structure in the mantle transition zone. *Physics of the Earth and Planetary Interiors*, *170*(3), 193–200.
Yoshino, T., Shimojuku, A., Shan, S., Guo, X., Yamazaki, D., Ito, E., … Funakoshi, K.-I. (2012). Effect of temperature, pressure and iron content on the electrical conductivity of olivine and its high-pressure polymorphs. *Journal of Geophysical Research*, *117*, B08205. https://doi.org/10.1029/2011JB008774
Zhang, B., Yoshino, T., Wu, X., Matsuzaki, T., Shan, S., & Katsura, T. (2012). Electrical conductivity of enstatite as a function of water content: Implications for the electrical structure in the upper mantle. *Earth and Planetary Science Letters*, *357*, 11–20.
Zhao, C., & Yoshino, T. (2016). Electrical conductivity of mantle clinopyroxene as a function of water content and its implication on electrical structure of uppermost mantle. *Earth and Planetary Science Letters*, *447*, 1–9.